Chinese Journal of Electronics
Vol.32, No.5, Sept. 2023

Microwave Tomographic Imaging of Anatomically Realistic Numerical Phantoms with Debye Dispersion for Breast Cancer Detection Using a Regularized Inverse Scattering Technique in the Time Domain

LIU Guangdong

(*School of Electrical and Control Engineering, Nanjing Polytechnic Institute, Nanjing 210048, China*)

Abstract — In recent years, three similar versions of time-domain inverse scattering (TDIS) algorithms have been proposed for the successful estimation of the dispersive dielectric properties of several single-pole Debye media. For practical applications in common biomedical engineering, an improved TDIS algorithm is explicitly derived to provide a more versatile algorithm for the microwave tomographic imaging of biological tissues. Its three improvements are as follows. The number of poles for Debye models is extended from one to a positive integer W. The second improvement is the extension of unknowns from three to $2W+2$ for each discretized cell. The third improvement is the adoption of the first-order Tikhonov regularization scheme. Based on the four classes of 2-dimensional anatomically realistic numerical phantoms with two-pole Debye dispersion from the University of Wisconsin Computational Electromagnetics Laboratory (UWCEM) database, the performance of the developed algorithm for the detection of a 3-mm-diameter tumor implanted in the four types of breast models was investigated for three scenarios. The obtained results preliminarily indicate that the modified technique is feasible and promising for the quantitative reconstruction of sparse breast tissues.

Key words — Biological tissues, Conjugate gradient methods, Finite-difference time-domain (FDTD) methods, Microwave imaging, Regulators.

I. Introduction

Breast cancer is the second leading cause of cancer death in America [1]. Accordingly, special attention has been given to advances in biomedical imaging [2]–[4]. Microwave imaging is of interest due to its advantages in nonionizing radiation and relatively inexpensive cost compared to conventional screening methods such as X-ray mammography and magnetic resonance imaging (MRI), and thus is considered an alternative technique for the near future [5].

Three classes of microwave imaging methods, viz., active, passive, and hybrid approaches, have been proposed for a variety of application areas thus far [6]–[10]. Among them, active microwave imaging methods have been followed with close interest for several decades [5], [10]–[12]. Usually, ongoing active methods may be divided into two subclasses. One includes radar-based approaches [13], [14], and the other includes tomographic approaches [4]. For both subclasses, some promising results have been obtained [4], [9]. The purpose of the former is to generate an image of the relative backscattered strength [15], [16], whereas that of the latter is to reconstruct the distribution of the quantitative dielectric parameters in its problem space [17], [18].

In microwave tomography, the resulting electromagnetic (EM) inverse scattering problems must be solved. Methodologically, these problems can be solved in the frequency domain [17], or the time domain [18]. To effectively detect small tumors in the early stage of breast cancer, time-domain, multifrequency, frequency-hopping, or wideband techniques are preferred in the case of limited-view configurations [19]–[21]. This paper is an improved version of several similar time-domain

Manuscript Received Sept. 16, 2021; Accepted Sept. 27, 2022. This work was supported by the National Natural Science Foundation of China (51271059) and the Natural Science Foundation of Nanjing Polytechnic Institute (NJPI-2022-06).
 DOI:10.23919/cje.2021.00.343

algorithms [18], [22], [23]. To date, a few algorithms have been proposed in the time domain for some frequency-independent media, such as the optimization approach based on wave splitting by Gustafsson *et al.* [24], the forward-backward time-stepping (FBTS) method by Takenaka *et al.* [20], the Lagrange multiplier-based optimization technique by Rekanos [25], and the time-domain Born iterative method (BIM) by Ali *et al.* [26]. In the first three algorithms above, a set of gradients was derived in closed form, which can be used conveniently in solving inverse problems by any of the gradient methods.

It is well known, however, that the dielectric properties of biological tissues are dispersive. For normal and malignant breast tissues, dispersive characteristics have been accurately described by one- and two-pole Debye models in the frequency range of 0.5–20 GHz, a single-pole Debye model from 3.1 to 10.6 GHz [27], and a four-pole Cole–Cole model from 10 Hz to 100 GHz [28]. Unfortunately, for Cole–Cole dispersive media, few existing inverse methods are directly available.

Currently, there are three similar versions of EM inverse scattering algorithms for the estimation of the dispersion properties of some single-pole Debye media. The first version is a voxel-based time-domain inverse scattering (TDIS) algorithm proposed by Winters *et al.* (called TDIS-W) [22], whereas the relaxation time τ is assumed to be a known constant. The second version was improved by Fhager *et al.* (called TDIS-F) [18] and is slightly different from the first version in that it introduces corresponding scaling factors. The third algorithm was developed by Papadopoulos *et al.* (called TDIS-P) [23] and differs from the first two algorithms in that the relaxation time τ is reconstructed simultaneously and that σ_s is neglected. Additionally, the first algorithm obviously differs from the latter two algorithms in the addition of a term related to the squared difference.

As discussed above, with single-pole Debye models, all three algorithms exhibit several obvious advantages, compared to the aforementioned algorithms. However, they still suffer from three common imperfections. First, there are no regularization terms, some classes of regularization schemes, such as deterministic edge-preserving regularization [29] and Tikhonov regularization [30], should be incorporated to cope with their ill-posedness. Second, none could reconstruct all four unknowns (ε_∞, $\Delta\varepsilon$, σ_s, and τ) for each voxel simultaneously. Finally, these algorithms cannot be directly applied to multiple-pole Debye dispersive media.

In this paper, an improved version of the TDIS algorithm is explicitly derived to provide a more versatile tool for the microwave tomographic imaging of biological tissues. Three improvements are given as follows. First, the number of poles in Debye models is extended from one to a positive integer W. The second improvement is the extension of unknowns from three to $2W+2$ for each discretized cell. The third improvement is the adoption of the first-order Tikhonov regularization scheme. Furthermore, based on four classes of anatomically realistic numerical phantoms with two-pole Debye dispersion from the UWCEM (University of Wisconsin Computational Electromagnetics Laboratory) database [31], the performance of the improved algorithm for the detection of 3-mm-diameter tumors in breasts with different densities is systematically researched.

II. Time-Domain Microwave Tomography Algorithm for Biological Tissues

In this section, based on the derivation described in [22] and [25], the author develops an improved TDIS algorithm.

1. Problem statement

Suppose that a microwave tomography problem space with a known boundary shape and position and its background space are denoted V and D, respectively. It is also assumed that the background space is filled with some media whose dielectric properties are known, whereas the problem space contains certain biological tissues with partially unknown dielectric properties, that all the media within V and D are nonmagnetic, linear, time-invariant and isotropic, and that the relative permittivity with a complex value, for each biological tissue located at point $\boldsymbol{r}$ within V is given by a W-pole Debye equation as reference [27].

In addition, this versatile Debye model can be easily simplified into several special cases as follows: If $W=1$, it would be reduced into a single-pole Debye model, the same as [22] and also similar to [18]; If $W=1$ and $\sigma_s=0$, it would be turned into a single-pole Debye model in the same manner as [23]; However, if $\Delta\varepsilon_w=0$, it could be degraded into a nondispersive model similar to references [20], [24], [25].

According to an idea similar to that of [23], when the ith microwave-transmitting antenna located at $\boldsymbol{r}_i$ within D is activated, all the Debye model parameters are explicitly shown in the following time-domain Maxwell differential equations:

$$\nabla\times\boldsymbol{H}_i(\boldsymbol{r},t)-\varepsilon_0\varepsilon_\infty(\boldsymbol{r})\,\partial_t\boldsymbol{E}_i(\boldsymbol{r},t) -\sigma_s(\boldsymbol{r})\,\boldsymbol{E}_i(\boldsymbol{r},t)-\sum_{w=1}^{W}\boldsymbol{J}_{i,w}(\boldsymbol{r},t)-\boldsymbol{J}_i(\boldsymbol{r},t)=\boldsymbol{0} \quad (1)$$

$$\nabla\times\boldsymbol{E}_i(\boldsymbol{r},t)+\mu_0\partial_t\boldsymbol{H}_i(\boldsymbol{r},t)=\boldsymbol{0} \quad (2)$$

and a set of (W) auxiliary differential equations:

$$\boldsymbol{J}_{i,w}(\boldsymbol{r},t)+\tau_w(\boldsymbol{r})\,\partial_t\boldsymbol{J}_{i,w}(\boldsymbol{r},t)-\varepsilon_0\Delta\varepsilon_w(\boldsymbol{r})\,\partial_t\boldsymbol{E}_i(\boldsymbol{r},t)=\boldsymbol{0} \tag{3}$$

where $\boldsymbol{r}\in V\cup D$, $t\in[0,T]$, T denotes the time interval for measurement, ∇ represents the Hamilton operator, ∂_t represents 1st-order temporal partial differential operator, μ_0 is the free-space permeability, $\boldsymbol{H}_i(\boldsymbol{r},t)$, $\boldsymbol{E}_i(\boldsymbol{r},t)$, and $\boldsymbol{J}_{i,w}(\boldsymbol{r},t)$ are the magnetic field intensity, electric field intensity, and dispersion current density of the wth pole, respectively, and an imposed source current density $\boldsymbol{J}_i^{\mathrm{s}}(\boldsymbol{r},t)=\delta_{\mathrm{Dirac}}(\boldsymbol{r}-\boldsymbol{r}_i)\,s(t)$, where δ_{Dirac} is the Dirac delta function and $s(t)$ is a time-domain signal.

The imaging objective is hence to estimate $2W+2$ Debye model parameters using measured data in the time domain. For this reason, a vector is predefined as $\boldsymbol{p}=[\varepsilon_\infty,\sigma_s,\Delta\varepsilon_1,\ldots,\Delta\varepsilon_W,\tau_1,\ldots,\tau_W]^{\mathrm{T}}$, in which the superscript T is a transpose operator. Consequently, if N represents the total number of cells (voxels) to be discretized within the problem space V, then we have $N(2W+2)$ unknowns for the imaging problem.

2. Constrained minimization problem

According to similar common practices such as those presented in [20]–[25], the imaging problem can be formulated as the following constrained minimization problem:

$$\begin{cases}\boldsymbol{p}=\arg\min\limits_{\boldsymbol{p}}\{F[\boldsymbol{E}(\boldsymbol{p})]\}\\ \text{s.t. Equations (1) to (3)}\end{cases} \tag{4}$$

where its cost functional F, which is usually nonlinear with respect to the unknown vector $\boldsymbol{p}$, is given by

$$F[\boldsymbol{E}(\boldsymbol{p})]=\frac{1}{2}\sum_{i=1}^{I}\sum_{j=1}^{J}\int_0^T\left\|\boldsymbol{E}_{i,j}(\boldsymbol{p})-\boldsymbol{E}_{i,j}^{\mathrm{m}}\right\|_2^2\mathrm{d}t+\frac{1}{2}\sum_{l=1}^{2W+2}\gamma_l\int_V\|\nabla p_l\|_2^2\,\mathrm{d}\boldsymbol{r} \tag{5}$$

On the right-hand side of (5), the first term describes the squared residual between the measured electric fields $\boldsymbol{E}_{i,j}$ and the computed electric fields $\boldsymbol{E}_{i,j}(\boldsymbol{p})$ for current $\boldsymbol{p}$ at the jth receiving antenna due to the activation of the ith transmitting antenna spanning from 0 to T, where I and J are the total numbers of transmitters and receivers, respectively, and the second term denotes the first-order Tikhonov regularization [30], [32], in which p_l and γ_l are the lth components of $\boldsymbol{p}$ and $\boldsymbol{\gamma}$, respectively, and the regularization vector $\boldsymbol{\gamma}=[\gamma_1,\gamma_2,\ldots,\gamma_{2W+2}]^{\mathrm{T}}$.

Similar to references [18], [23], but different from [22], [25], there is not an error term with respect to magnetic fields; this can greatly reduce the difficulty in measuring electric fields and magnetic fields simultaneously. In addition, a similar regularization scheme has been adopted, as in [25], although it does not appear in references [18], [22], [23]. Moreover, similar to [33], because each component of $\boldsymbol{p}$ can make different contributions to F, the author applies $2W+2$ separate regularization factors in this paper, whereas only a single factor is used in [25]. Additionally, it is challenging to find their optimal values with methods such as the L-curve [34]. This regularization scheme can also be dropped easily by specifying $\boldsymbol{\gamma}=0$.

3. Unconstrained minimization problem

Using the augmented Lagrangian method [35], the author transforms the above problem into the following unconstrained minimization problem:

$$\boldsymbol{p}=\arg\min_{\boldsymbol{p}}\{F^{\mathrm{a}}[\boldsymbol{E}(\boldsymbol{p}),\boldsymbol{e}(\boldsymbol{p})]\} \tag{6}$$

where the augmented cost functional F^{a} is denoted

$$\begin{aligned}&F^{\mathrm{a}}[\boldsymbol{E}(\boldsymbol{p}),\boldsymbol{e}(\boldsymbol{p})]\\&=F[\boldsymbol{E}(\boldsymbol{p})]+\sum_{i=1}^{I}\int_0^T\int_{V\cup D}\Big[\boldsymbol{e}_i\cdot\Big(\nabla\times\boldsymbol{H}_i\\&\quad-\varepsilon_0\varepsilon_\infty\partial_t\boldsymbol{E}_i-\sigma_{\mathrm{s}}\boldsymbol{E}_i-\sum_{w=1}^{W}\boldsymbol{J}_{i,w}-\boldsymbol{J}_i\Big)\\&\quad+\boldsymbol{h}_i\cdot(\nabla\times\boldsymbol{E}_i+\mu_0\partial_t\boldsymbol{H}_i)\\&\quad+\sum_{w=1}^{W}\boldsymbol{q}_{i,w}\cdot(\boldsymbol{J}_{i,w}+\tau_w\partial_t\boldsymbol{J}_{i,w}-\varepsilon_0\Delta\varepsilon_w\partial_t\boldsymbol{E}_i)\Big]\mathrm{d}\boldsymbol{r}\mathrm{d}t\end{aligned} \tag{7}$$

where $\boldsymbol{e}_i$, $\boldsymbol{h}_i$, and $\boldsymbol{q}_{i,w}$ are the Lagrangian vector multipliers corresponding to $\boldsymbol{E}_i$, $\boldsymbol{H}_i$, and $\boldsymbol{J}_{i,w}$, respectively.

4. Gradients

Solving the resulting unconstrained minimization problem by using the variational method [36], we obtain $\delta F^{\mathrm{a}}=0$, where δ is the first-order variation operator. After some calculation procedures similar to [22], [23], [25], one can determine that a set of multipliers, $\boldsymbol{e}_i$, $\boldsymbol{h}_i$, and $\boldsymbol{j}_{i,w}=-\varepsilon_0\Delta\varepsilon_w\partial_t\boldsymbol{q}_{i,w}$, must satisfy the adjoint equations over the time interval $[T,0]$, shown as

$$\nabla\times\boldsymbol{h}_i+\varepsilon_0\varepsilon_\infty\partial_t\boldsymbol{e}_i-\sigma_{\mathrm{s}}\boldsymbol{e}_i-\sum_{w=1}^{W}\boldsymbol{j}_{i,w}+\sum_{j=1}^{J}\left(\boldsymbol{E}_{i,j}-\boldsymbol{E}_{i,j}^{\mathrm{m}}\right)=\boldsymbol{0} \tag{8}$$

$$\nabla\times\boldsymbol{e}_i-\mu_0\partial_t\boldsymbol{h}_i=\boldsymbol{0} \tag{9}$$

$$\boldsymbol{j}_{i,w}-\tau_w\partial_t\boldsymbol{j}_{i,w}+\varepsilon_0\Delta\varepsilon_w\partial_t\boldsymbol{e}_i=\boldsymbol{0} \tag{10}$$

The $2W+2$ analytic gradients, namely, Fréchet derivatives of F^{a} with respect to p_l, at every position within V are given by

$$g_{\varepsilon_\infty} = -\varepsilon_0 \sum_{i=1}^{I} \int_0^T (\boldsymbol{e}_i \cdot \partial_t \boldsymbol{E}_i) \mathrm{d}t - \gamma_1 \nabla^2 \varepsilon_\infty \tag{11}$$

$$g_{\sigma_s} = -\sum_{i=1}^{I} \int_0^T (\boldsymbol{e}_i \cdot \boldsymbol{E}_i) \mathrm{d}t - \gamma_2 \nabla^2 \sigma_s \tag{12}$$

$$g_{\Delta\varepsilon_w} = -\varepsilon_0 \sum_{i=1}^{I} \int_0^T (\boldsymbol{j}_{i,w} \cdot \partial_t \boldsymbol{E}_i) \mathrm{d}t - \gamma_{w+2} \nabla^2 \Delta\varepsilon_w, \text{ and} \tag{13}$$

$$g_{\tau_w} = \sum_{i=1}^{I} \int_0^T (\boldsymbol{j}_{i,w} \cdot \partial_t \boldsymbol{J}_{i,w}) \mathrm{d}t - \gamma_{w+W+2} \nabla^2 \tau_w \tag{14}$$

where ∇^2 is the Laplace operator. Then, one can easily obtain the gradient vector $\boldsymbol{g}$ defined by

$$\boldsymbol{g} = [g_{\varepsilon_\infty}, g_{\sigma_s}, g_{\Delta\varepsilon_1}, \ldots, g_{\Delta\varepsilon_W}, g_{\tau_1}, \ldots, g_{\tau_W}]^{\mathrm{T}} \tag{15}$$

5. Direct and inverse algorithms

With these closed-form gradients, one can thus iteratively solve the original TDIS problem by any gradient method [37]. In each iteration of our TDIS algorithm, there are two subproblems to address. One is the direct scattering subproblem, and the other is the inverse scattering subproblem.

In this work, the finite-difference time-domain (FDTD) method is used as a direct solver [38], in which its FDTD solution space is terminated by the convolutional perfectly matched layer (CPML) [39], while the Polak–Ribière–Polyak (PRP) conjugate gradient (CG) method is adopted as an inverse solver [37].

As mentioned above, it is assumed that the problem space V is discretized into N cells and that the dielectric properties within each individual cell are constant. Let the position of the nth cell be denoted $\boldsymbol{r}_n$; then, $\boldsymbol{p}$ and $\boldsymbol{g}$ are rewritten in a discrete form as $\underline{\boldsymbol{p}} = [\boldsymbol{p}(\boldsymbol{r}_1), \boldsymbol{p}(\boldsymbol{r}_2), \ldots, \boldsymbol{p}(\boldsymbol{r}_n), \ldots, \boldsymbol{p}(\boldsymbol{r}_N)]^{\mathrm{T}}$ and $\underline{\boldsymbol{g}} = [\boldsymbol{g}(\boldsymbol{r}_1), \boldsymbol{g}(\boldsymbol{r}_2), \ldots, \boldsymbol{g}(\boldsymbol{r}_n), \ldots, \boldsymbol{g}(\boldsymbol{r}_N)]^{\mathrm{T}}$, respectively. Denoting the index of iterations k, at the kth iteration of the presented TDIS algorithm, the major steps of the direct and inverse algorithms are then summarized as follows.

Step 1 Given the current estimations of $\underline{\boldsymbol{p}}$, $\underline{\boldsymbol{p}}_k$, calculate the forward fields ($\boldsymbol{E}_i$, $\boldsymbol{H}_i$, and $\boldsymbol{E}_{i,w}$) by the FDTD method from equations (1)–(3).

Step 2 Compute the backward fields ($\boldsymbol{e}_i$, $\boldsymbol{h}_i$, and $\boldsymbol{j}_{i,w}$) by the FDTD method from equations (8)–(10).

Step 3 Solve equations (11)–(15) to obtain the current gradient $\underline{\boldsymbol{g}}_k$.

Step 4 Compute the current direction vector $\underline{\boldsymbol{d}}_k$ for the PRP CG method by the solution to the following equation as [37].

Step 5 Compute the current step-size parameter λ_k for the PRP CG method by solving the line-search minimization problem as [40].

Step 6 Update the estimate for the next iteration as [37], and if necessary, use the known a priori actual parameter $\underline{\boldsymbol{p}}$ to calculate the current relative root mean squared error (RMSE) e, defined by

$$e(k) = \|\underline{\boldsymbol{p}}_k - \underline{\boldsymbol{p}}\|_2 / \|\underline{\boldsymbol{p}}\|_2 \tag{16}$$

Step 7 Stop if a prespecified iteration number k_{pre} or an error threshold e_{th} is reached; otherwise, $k = k + 1$, and return to step 1.

The key steps of the microwave tomographic imaging algorithm are illustrated in Fig.1.

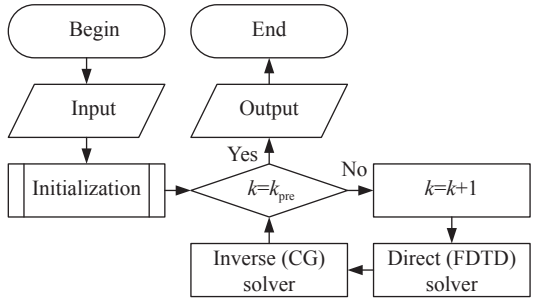

Fig. 1. Basic flowchart of the proposed TDIS technology.

III. Application in Breast Cancer Detection

The FBTS algorithm was successfully applied first in the detection of several tumors within a simple two-dimensional (2-D) breast model from a synthetic dataset [20], and then in the detection of a 5-mm-diameter tumor, an anatomically realistic 2-D breast model from a magnetic resonance imaging (MRI) dataset was added [11]. Unfortunately, neither breast model introduced the dispersive properties of breast tissues.

By using a single-pole Debye model, a region-based TDIS algorithm was developed to successfully estimate the spatially averaged Debye parameters within an MRI-derived 2-D breast phantom [22], while a pixel-based TDIS algorithm was presented to reconstruct the spatial distribution of Debye parameters from a synthetic 2-D numerical breast model [18]. However, in both algorithms, the simulated measurement data were not contaminated by any noise.

To initially test the feasibility and robustness of our improved algorithm for the early detection of breast cancer, we applied it to four classes of 2-D numerical breast models with various densities and structures, which were all implanted into a 3 mm diameter tumor, for three different scenarios.

1. Breast models

To date, several numerical breast models, such as a simple 2-D model [20], the anatomically realistic 2-D

phantoms [11], [22], a relatively simple three-dimensional (3-D) phantom [41], or anatomically realistic 3-D phantoms [12], [31], [42], have been used in FDTD simulations. Among them, a set of 3-D numerical breast phantoms developed by Zastrow *et al.* are relatively accurate and well-accepted. These phantoms can be found from a free online repository provided by the UWCEM research group [31]. They are realistic, both anatomically and dielectrically [31], [42]. Moreover, according to the definitions of the American College of Radiology (ACR) [43], these models are classified into four classes: 1) ACR-I, which includes mostly fatty breast tissue; 2) ACR-II, which includes scattered fibroglandular (FG) breast tissue; 3) ACR-III, which includes heterogeneously dense breast tissue; and 4) ACR-IV, which includes very dense breast tissue [31], [42]. These numerical models, whose cubic cells are all 0.5 mm × 0.5 mm × 0.5 mm in size, include layers of skin, subcutaneous fat, and muscle chest wall, with thicknesses of approximately 1.5 mm, 1.5 cm, and 0.5 cm, respectively. An immersion medium was assigned to all voxels outside of each breast.

Usually, the larger the value of W is, the smaller the modeling error but the higher the computational cost. A good W candidate takes the value that balances the modeling error and the computational cost. Based on a two-pole ($W = 2$) model with fixed τ_1 and τ_2 values of 7.22 ps and 15.30 ps, over the 0.5–20.0 GHz band, four breast phantoms, with identifiers (IDs) of 071904, 010204, 070604PA2, and 012304, from ACR-I, ACR-II, ACR-III, and ACR-IV, respectively, are selected first. Then a malignant spherical 3-mm-diameter tumor is implanted with two-pole Debye parameters given by $\varepsilon_\infty = 6.75$, $\sigma_s = 0.79$ S/m, $\Delta\varepsilon_1 = 25.61$, and $\Delta\varepsilon_2 = 23.91$ [27]. Then, four individual coronal slices are taken directly as the first group of corresponding 2-D versions of cancerous numerical breast models with a square cell size of 0.5 mm × 0.5 mm, labeled E, F, G, and H. Last, this group of models is extracted as the second group of models with a square cell size of 1.0 mm × 1.0 mm, labeled A, B, C, and D.

2. Measurement setup

A bistatic measurement system consisting of a 4-element transmitting antenna array ($I = 4$) and a 28-element receiving antenna array ($J = 28$) is adopted in this work. It is assumed that all the elements are modeled as dipoles located uniformly on a rectangle that surrounds the problem space V. Each transmitting antenna element takes turns to illuminate the problem space by the incident transverse magnetic (TM) waves generated by a z-direction line current source, whose ultrawideband (UWB) sinusoidally modulated Gaussian excitation pulse signal is given by

$$s(t) = \sin(2\pi f_c t)\exp[-(t-t_2)^2/(t_1)^2] \tag{17}$$

where $t_1 = 100.0$ ps, $t_2 = 4.0\,t_1$, the center frequency $f_c = 3.2$ GHz.

We apply the FDTD method with a time step size $\Delta t_1 = 0.59$ ps to the first group of 2-D phantoms E, F, G, and H, forming four sets of numerical "measured" total electric fields within 2.83 ns. Then, suppose that the skin, immersion medium, CPML, FG tissue, transitional tissue, fatty tissue, and malignant tumor are labeled by media numbers coded −2, −1, 0, 1, 2, 3, and 4, respectively. Fig.2 shows the corresponding spatial distributions of our data acquisition systems related to media numbers in the four 2-D phantoms. In each subgraph, an additional four pink dots, twenty-eight green dots, and one blue rectangular line mark the locations of transmitting antenna elements, receiving antenna elements, and boundaries of imaging spaces for later inverse procedures, respectively.

For phantoms E, F, G, and H, the position coordinates of the tumor center, four transmitting array elements, and twenty-eight receiving array elements are summarized in Table 1. For each phantom, after all the receiving antenna elements record total electric fields, the acquisition of these fields can form 4 × 28 (= 112) transmitter/receiver combinations as a set of measurement data.

3. Reconstructions

The step-by-step solution procedure shown in Fig.1 is utilized to estimate the spatial distributions of the two-pole Debye parameters (ε_∞, σ_s, $\Delta\varepsilon_1$, and $\Delta\varepsilon_2$) from the second group of 2-D cancerous numerical breast models (A, B, C, and D), based on the following three specific scenarios.

Scenario I It is assumed that the thickness, location, and average Debye parameters of the skin region are estimated by the improved skin-sensing method [44], the breast surface identification (BSID) technique [45], and the region-based TDIS algorithm [22], respectively, that the measured fields are not corrupted by any noise, that the regularization scheme is not adopted (namely, $\gamma = 0$) and that the initial estimates of Debye parameters (ε_∞, σ_s, $\Delta\varepsilon_1$, and $\Delta\varepsilon_2$) are chosen to be equal to 1+10% of their actual values [27] for the skin region and the same as those in the immersion medium for other regions [31], [42].

Scenario II Similar to Scenario I, suppose that the measured data are not contaminated by any noise and that the regularization scheme is not applied. The initial guesses for the Debye parameters in the entire region are set equal to those in the immersion medium.

Scenario III The additive white Gaussian noise (AWGN) with a signal-to-noise ratio (SNR) of 20 dB is

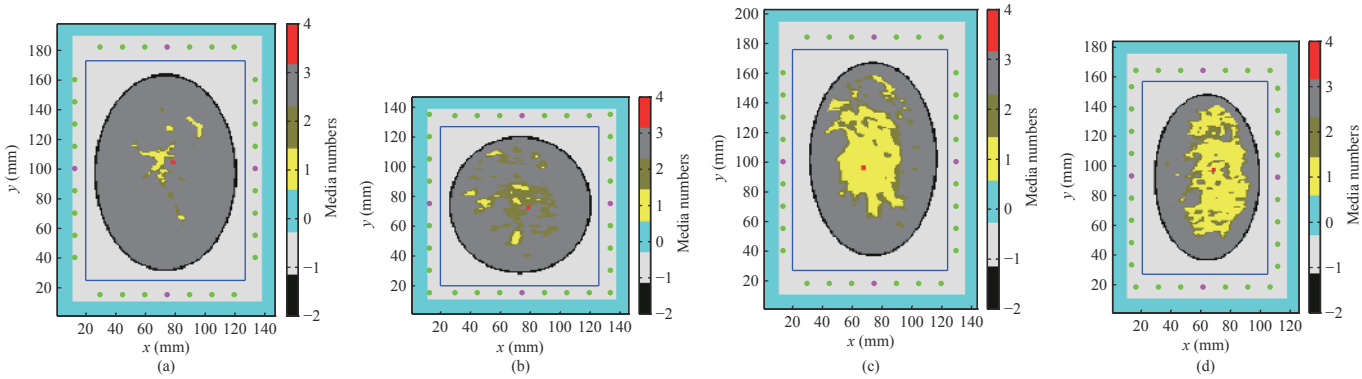

Fig. 2. Spatial distributions of data acquisition systems related to medium numbers in 2-D cancerous numerical breast phantoms (a) E, (b) F, (c) G, and (d) H, where medium numbers −2, −1, 0, 1, 2, 3, and 4 skin denote the immersion medium, CPML, FG tissue, transitional tissue, fatty tissue, and malignant tumor, respectively, and an additional four pink dots, twenty-eight green dots, and one blue rectangular line mark the locations of transmitting antenna elements, receiving antenna elements, and boundaries of problem spaces, respectively.

Table 1. Position coordinates (unit: mm) of the tumor center, four transmitting array elements, and twenty-eight receiving array elements for four breast phantoms

Phantom	Tumor center (x, y) (mm)	Four transmitters (x, y) (mm)	Twenty-eight receivers (x, y) (mm)
E	(78, 104)	(13, 100), (75, 182), (134, 100), (75, 15)	(13, 40), (13, 55), (13, 70), (13, 85), (13, 115), (13, 130), (13, 145), (13, 160), (30, 182), (45, 182), (60, 182), (90, 182), (105, 182), (120, 182), (134, 40), (134, 55), (134, 70), (134, 85), (134, 115), (134, 130), (134, 145), (134, 160), (30, 15), (45, 15), (60, 15), (90, 15), (105, 15), (120, 15)
F	(78, 72)	(13, 75), (75, 134), (134, 75), (75, 15)	(13, 15), (13, 30), (13, 45), (13, 60), (13, 90), (13, 105), (13, 120), (13, 135), (30, 134), (45, 134), (60, 134), (90, 134), (105, 134), (120, 134), (134, 15), (134, 30), (134, 45), (134, 60), (134, 90), (134, 105), (134, 120), (134, 135), (30, 15), (45, 15), (60, 15), (90, 15), (105, 15), (120, 15)
G	(67, 96)	(14, 100), (75, 184), (130, 100),(75, 18)	(14, 40), (14, 55), (14, 70), (14, 85),(14, 115), (14, 130), (14, 145), (14, 160), (30, 184), (45, 184), (60, 184), (90, 184), (105, 184), (120, 184), (130, 40), (130, 55), (130, 70), (130, 85), (130, 115), (130, 130), (130, 145), (130, 160), (30, 18), (45, 18), (60, 18), (90, 18), (105, 18), (120, 18)
H	(68, 97)	(14, 93), (62, 164), (112, 92),(62, 18)	(14, 33), (14, 48), (14, 63), (14, 78), (14, 108), (14, 123), (14, 138), (14, 153), (17, 164), (32, 164), (47, 164), (77, 164), (92, 164), (107, 164), (112, 32), (112, 47), (112, 62), (112, 77), (112, 107), (112, 122), (112, 137), (112, 152), (17, 18), (32, 18), (47, 18), (77, 18), (92, 18), (107, 18)

incorporated into measurements, and all four parameters assumed to be equal are chosen by the L-curve method [34] to be approximately equal to 0.001 is used. Additionally, we assume that all the initial guesses for the three parameters are the same as those in Scenario II.

For breast phantoms A, B, C, and D, a time step size $\Delta t_2 = 1.18$ ps is adopted in all their direct FDTD solvers with the solution spaces consisting of 127 × 178, 126 × 127, 124 × 183, and 106 × 164 cells, respectively, while their problem spaces in their inverse solvers consist of 107 × 148, 106 × 107, 104 × 149, and 84 × 130 cells, respectively. For each FDTD simulation in this work, a ten-cell CPML absorber is applied to truncate its solution space.

In this paper, the selected criterion for stopping the algorithm is $k_{\text{pre}} = 300$, and imaging results are given in the next section.

IV. Results and Discussion

1. Scenario I

The spatial distributions of ε_∞, σ_s, and $\Delta\varepsilon_1$ (similar results for $\Delta\varepsilon_2$ are omitted due to limited space) for the 2-D cancerous breast phantom A, based on Scenario I, are given in Figs.3, 4 and 5, respectively. Similarly, Figs. 6–8, 9–11, and 12–14 give the corresponding distributions for phantoms B, C, and D, respectively. In these figures, the subgraphs (a), (b), (c), and (d) represent the actual distribution, initial guess, estimated value at the 300th iteration, and comparison between the original (black solid line) and reconstructed (blue dotted line) profiles on the x-axis through its tumor center, respectively. In particular, one additional green circle in each subgraph (c) marks the location and size of the actual tumor to examine the performance of the technique developed for breast cancer detection.

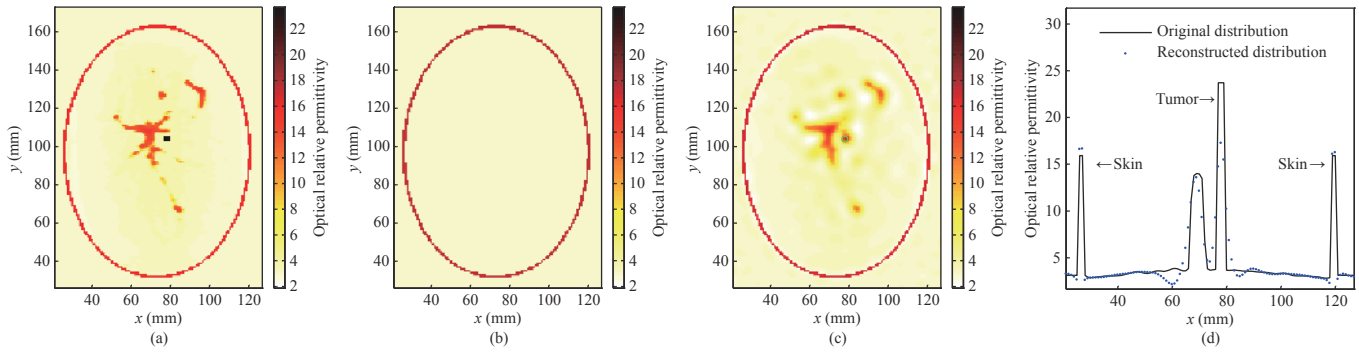

Fig. 3. (a) Original, (b) initial, (c) reconstructed at the 300th iteration, and (d) comparison between original (black solid line) and reconstructed (blue dotted line) profiles on the x-axis through the tumor center of ε_∞ in 2-D cancerous breast phantom **A** based on *Scenario I*.

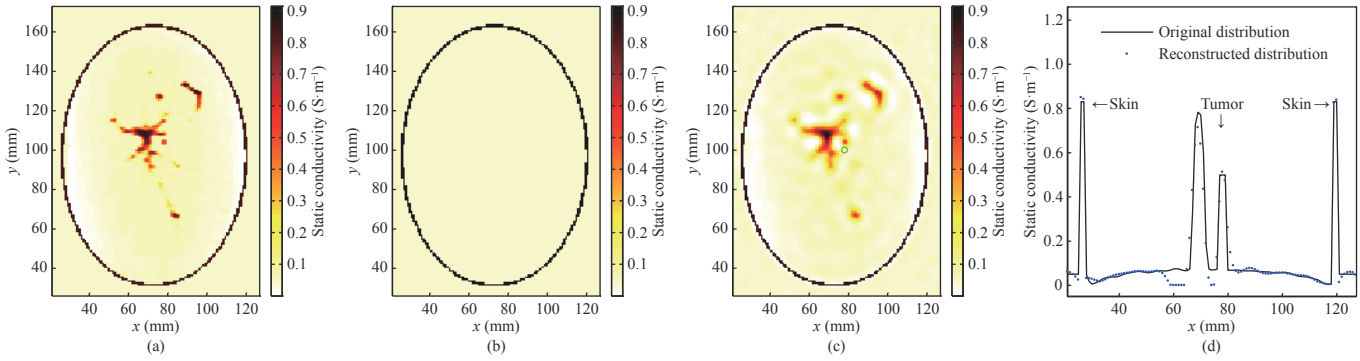

Fig. 4. (a) Original, (b) initial, (c) reconstructed at the 300th iteration, and (d) comparison between original (black solid line) and reconstructed (blue dotted line) profiles on the x-axis through the tumor center of σ_s in 2-D cancerous breast phantom **A** based on *Scenario I*.

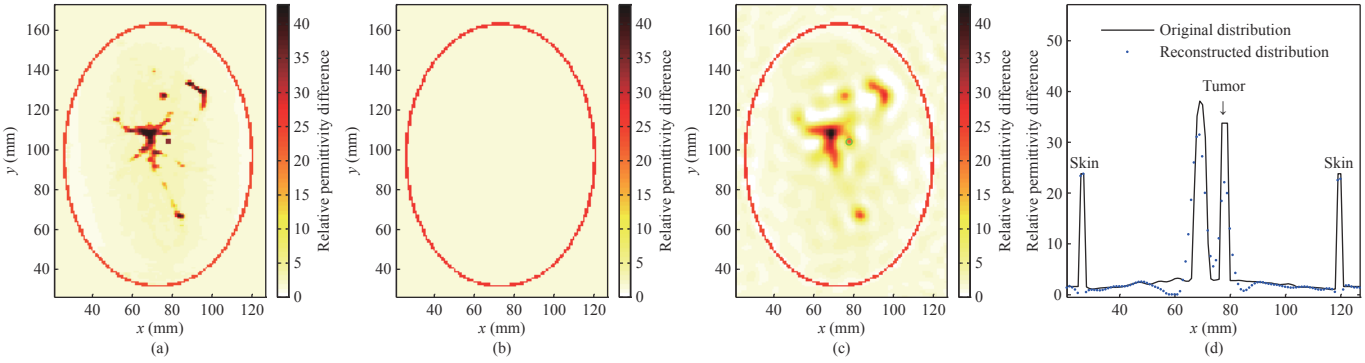

Fig. 5. (a) Original, (b) initial, (c) reconstructed at the 300th iteration, and (d) comparison between original (black solid line) and reconstructed (blue dotted line) profiles on the x-axis through the tumor center of $\Delta\varepsilon_1$ in 2-D cancerous breast phantom **A** based on *Scenario I*.

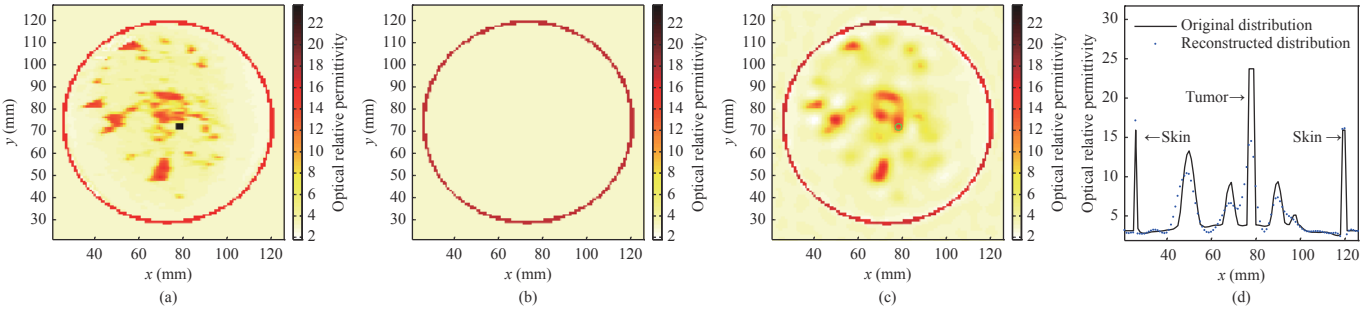

Fig. 6. (a) Original, (b) initial, (c) reconstructed at the 300th iteration, and (d) comparison between original (black solid line) and reconstructed (blue dotted line) profiles on the x-axis through the tumor center of ε_∞ in 2-D cancerous breast phantom **B** based on *Scenario I*.

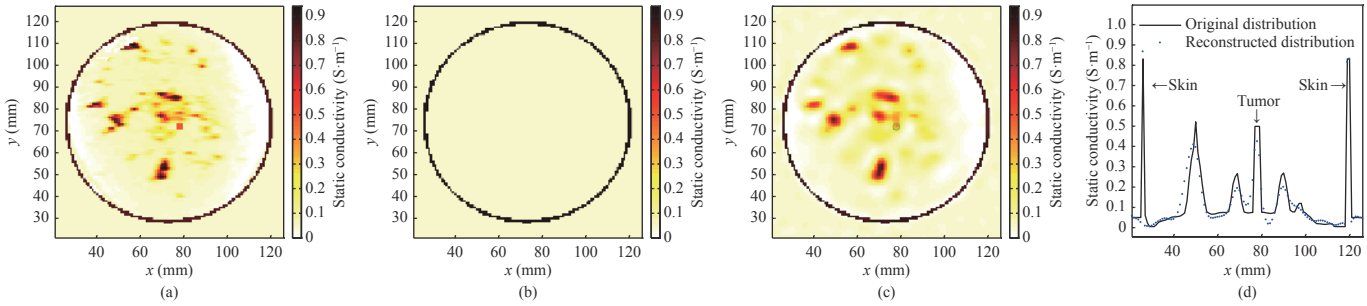

Fig. 7. (a) Original, (b) initial, (c) reconstructed at the 300th iteration, and (d) comparison between original (black solid line) and reconstructed (blue dotted line) profiles on the x-axis through the tumor center of σ_s in 2-D cancerous breast phantom **B** based on *Scenario I*.

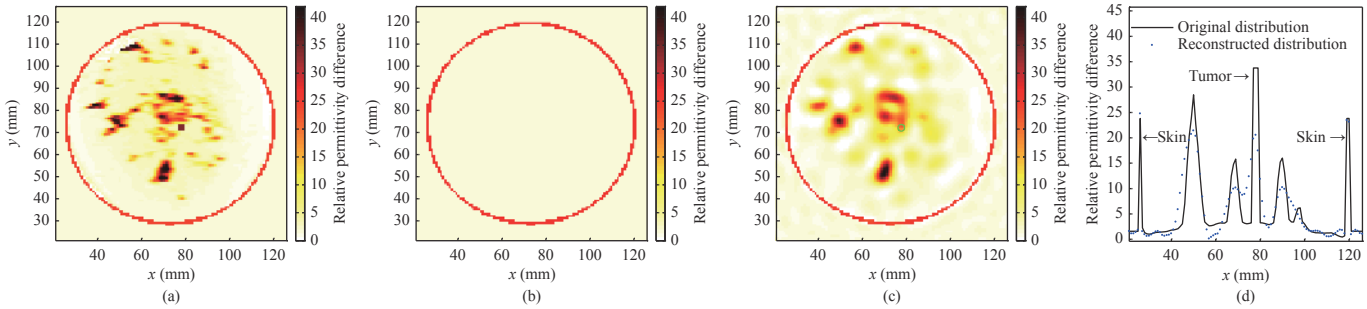

Fig. 8. (a) Original, (b) initial, (c) reconstructed at the 300th iteration, and (d) comparison between original (black solid line) and reconstructed (blue dotted line) profiles on the x-axis through the tumor center of $\Delta\varepsilon_1$ in 2-D cancerous breast phantom **B** based on *Scenario I*.

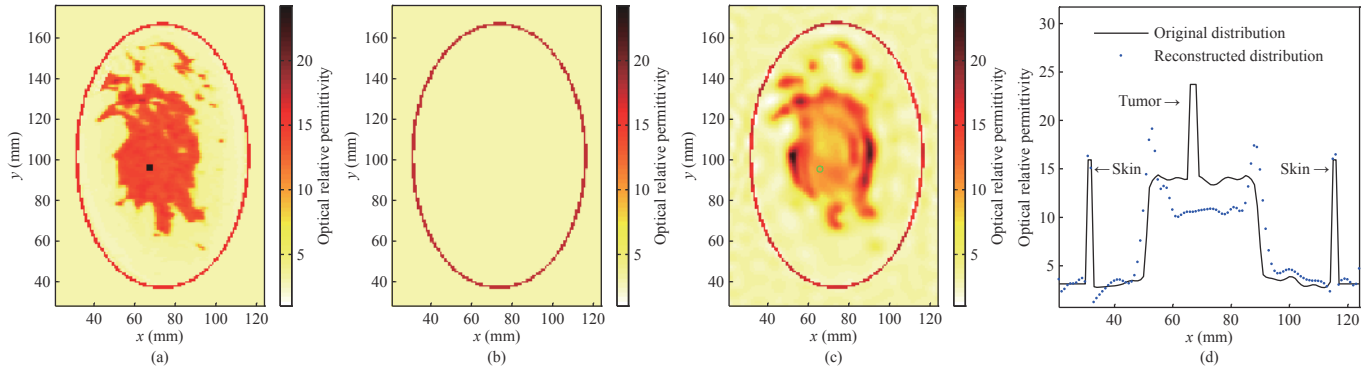

Fig. 9. (a) Original, (b) initial, (c) reconstructed at the 300th iteration, and (d) comparison between original (black solid line) and reconstructed (blue dotted line) profiles on the x-axis through the tumor center of ε_∞ in 2-D cancerous breast phantom **C** based on *Scenario I*.

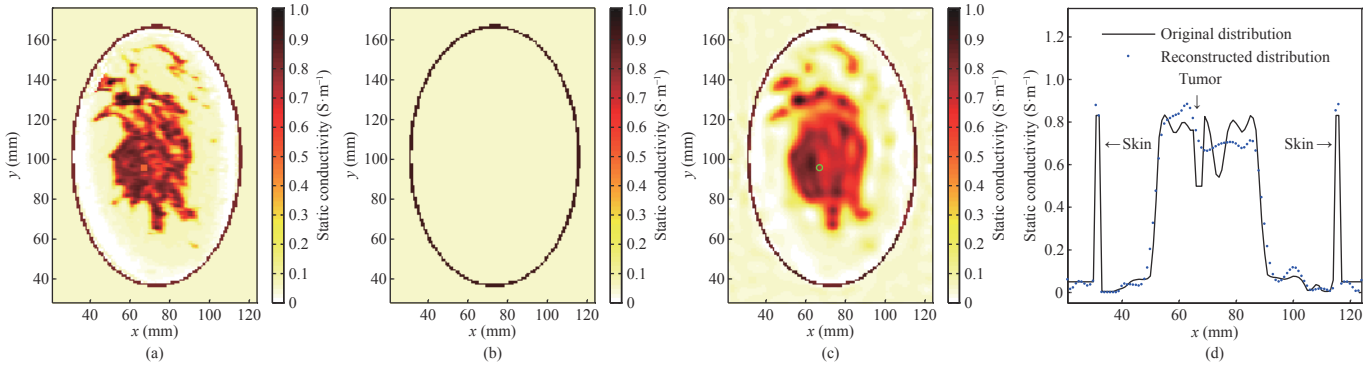

Fig. 10. (a) Original, (b) initial, (c) reconstructed at the 300th iteration, and (d) comparison between original (black solid line) and reconstructed (blue dotted line) profiles on the x-axis through the tumor center of σ_s in 2-D cancerous breast phantom **C** based on *Scenario I*.

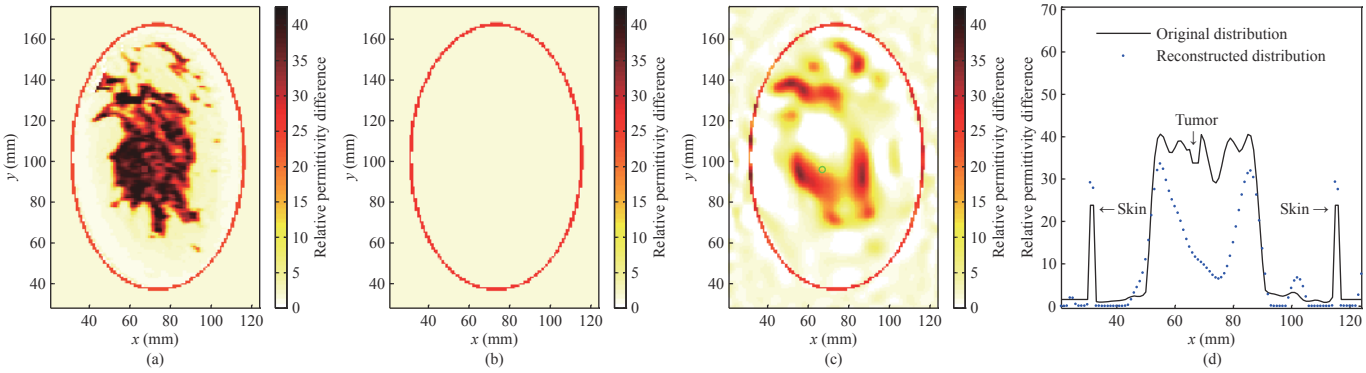

Fig. 11. (a) Original, (b) initial, (c) reconstructed at the 300th iteration, and (d) comparison between original (black solid line) and reconstructed (blue dotted line) profiles on the x-axis through the tumor center of $\Delta\varepsilon_1$ in 2-D cancerous breast phantom **C** based on *Scenario I*.

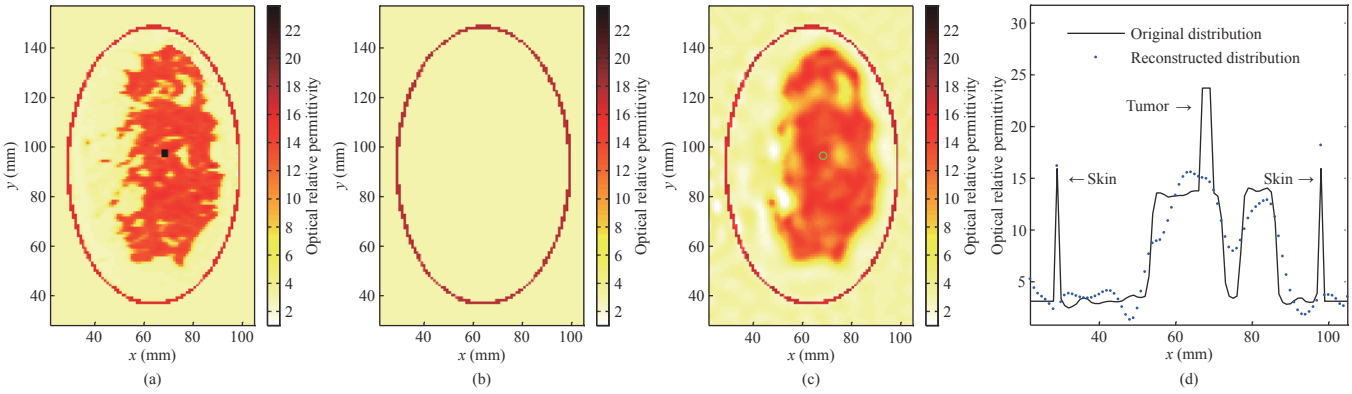

Fig. 12. (a) Original, (b) initial, (c) reconstructed at the 300th iteration, and (d) comparison between original (black solid line) and reconstructed (blue dotted line) profiles on the x-axis through the tumor center of ε_∞ in 2-D cancerous breast phantom **D** based on *Scenario I*.

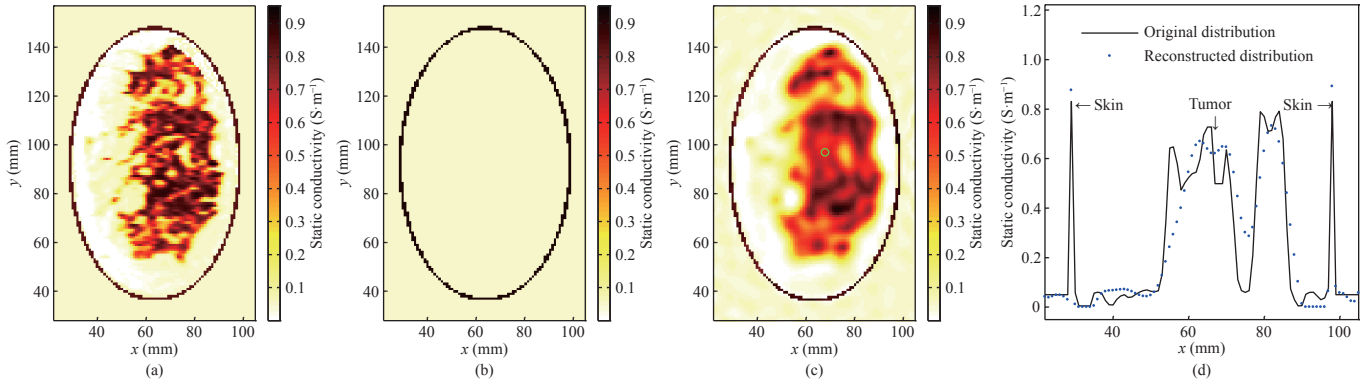

Fig. 13. (a) Original, (b) initial, (c) reconstructed at the 300th iteration, and (d) comparison between original (black solid line) and reconstructed (blue dotted line) profiles on the x-axis through the tumor center of σ_s in 2-D cancerous breast phantom **D** based on *Scenario I*.

As shown in Figs.3–5, the spatial distributions of the Debye model parameters in almost all of 2-D cancerous numerical breast phantom A are reconstructed successfully in Scenario I. In addition, a comparison among Figs.3–5 indicates that the estimation accuracy of σ_s is the best, followed by $\Delta\varepsilon_1$, and ε_∞ is the worst, which is similar to the findings presented by Winters *et al.* [22]. Breast phantom B is similar as breast phantom A, as shown in Figs.6–8, but the imaging accuracy decreases slightly. Figs.9–11 show that the imaging quality of the skin is the highest, that the imaging quality of normal tissues is the second highest, and that the tumor is the worst for breast phantom C. For breast phantom D, the reconstructed images shown in Figs.12–14 are seemingly poorer than those obtained by any other breast phantom.

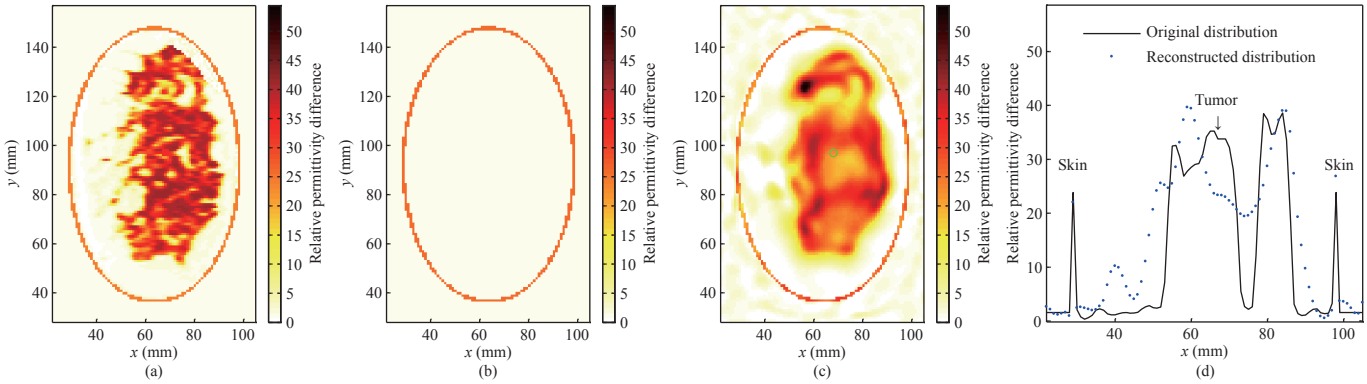

Fig. 14. (a) Original, (b) initial, (c) reconstructed at the 300th iteration, and (d) comparison between original (black solid line) and reconstructed (blue dotted line) profiles on the x-axis through the tumor center of $\Delta\varepsilon_1$ in 2-D cancerous breast phantom **D** based on *Scenario I*.

2. Scenario II

Based on Scenario II, Figs.15, 16, 17, and 18 show the spatial distributions of three two-pole Debye parameters (similar $\Delta\varepsilon_2$ results are omitted) in 2-D cancerous breast phantoms A, B, C, and D, respectively. In these figures, the subgraphs (a)–(c), (d)–(f), and (g)–(i) give the initial guess, estimated value at the 300th iteration, and comparison between the original (black solid line) and reconstructed (blue dotted line) profiles on the x-axis through its tumor center ε_∞, σ_s, and $\Delta\varepsilon_1$, respectively.

In particular, each additional green circle in subgraphs (b), (e), and (h) marks the location and size of the actual tumor.

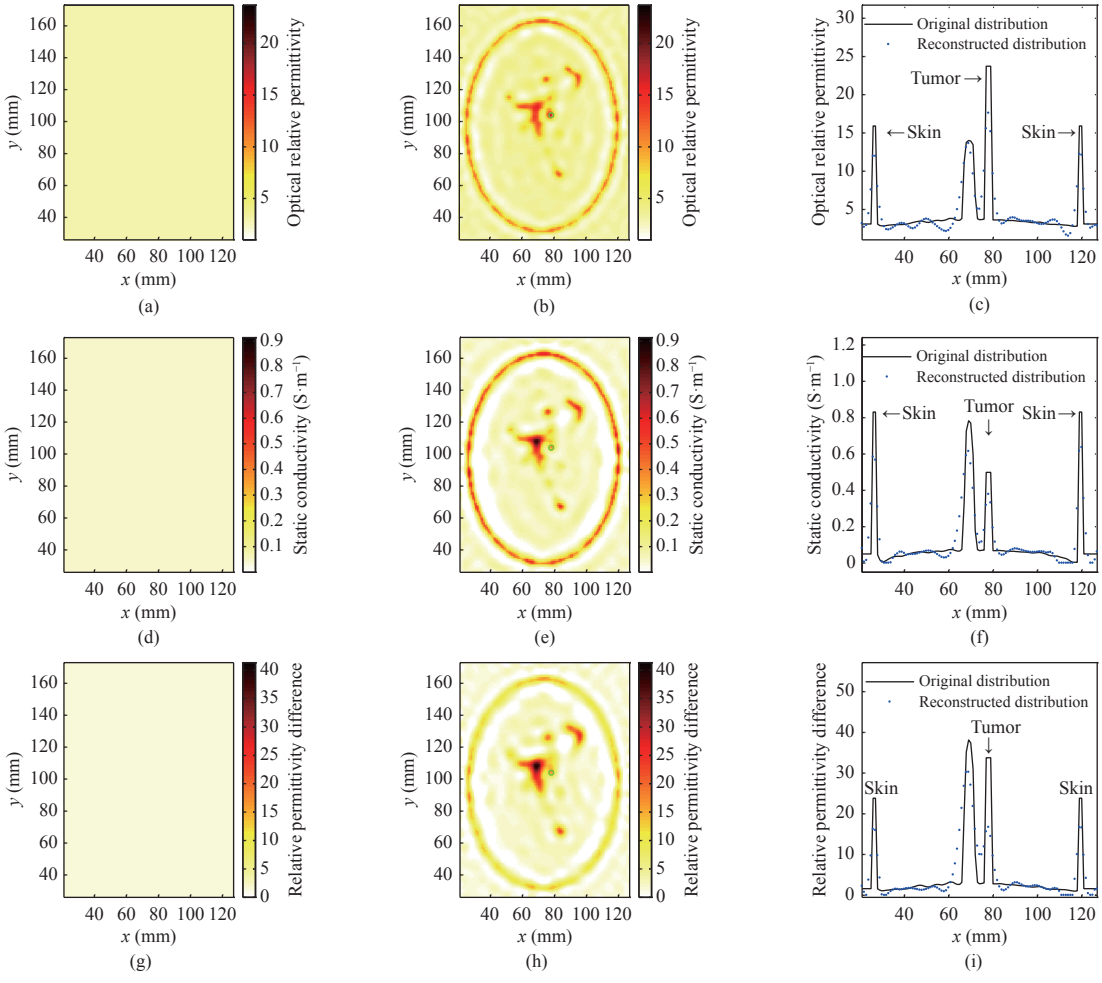

Fig. 15. Initial, reconstructed at the 300th iteration, and comparisons between original (black solid line) and reconstructed (blue dots) profiles on the x-axis through the tumor center for 2-D cancerous breast phantom **A** based on *Scenario II*: (a)–(c) ε_∞, (d)–(f) σ_s, and (g)–(i) $\Delta\varepsilon_1$.

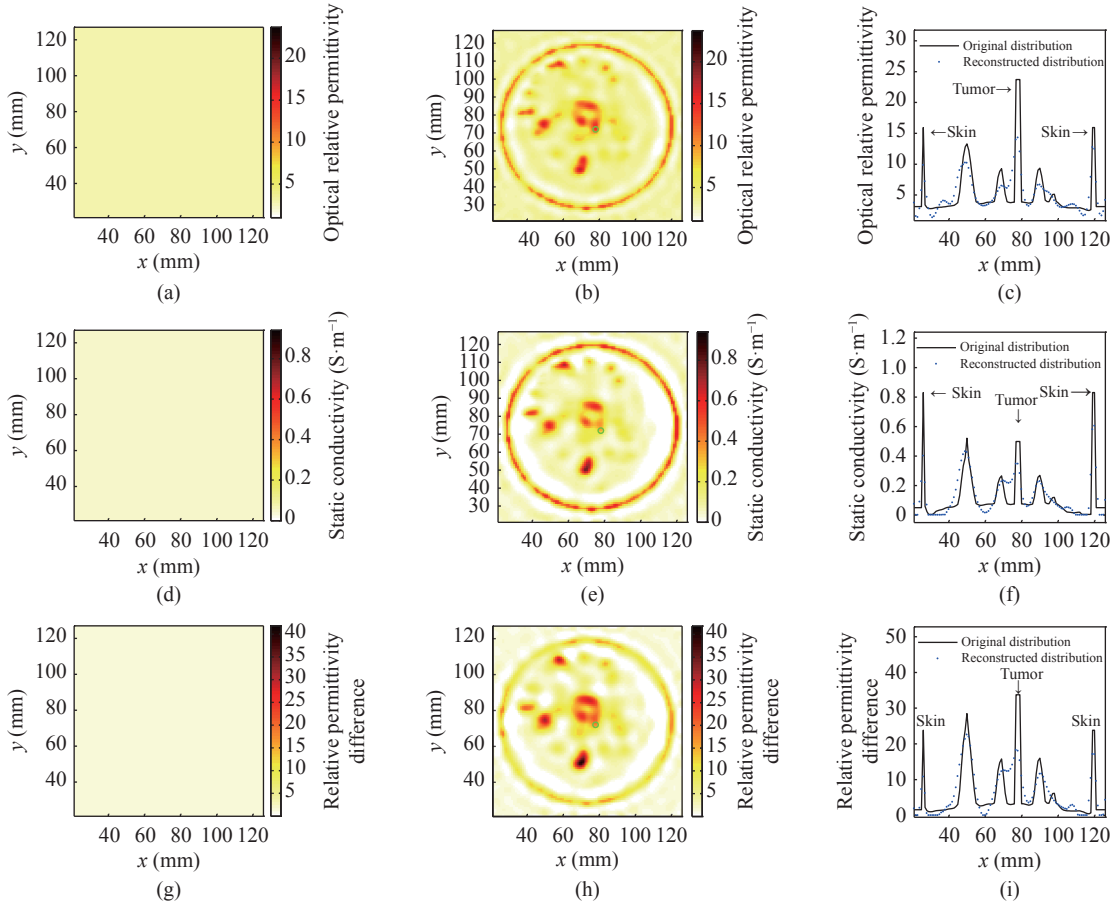

Fig. 16. Initial, reconstructed at the 300th iteration, and comparisons between original (black solid line) and reconstructed (blue dots) profiles on the x-axis through the tumor center for 2-D cancerous breast phantom **B** based on *Scenario II*: (a)–(c) ε_∞, (d)–(f) σ_s, and (g)–(i) $\Delta\varepsilon_1$.

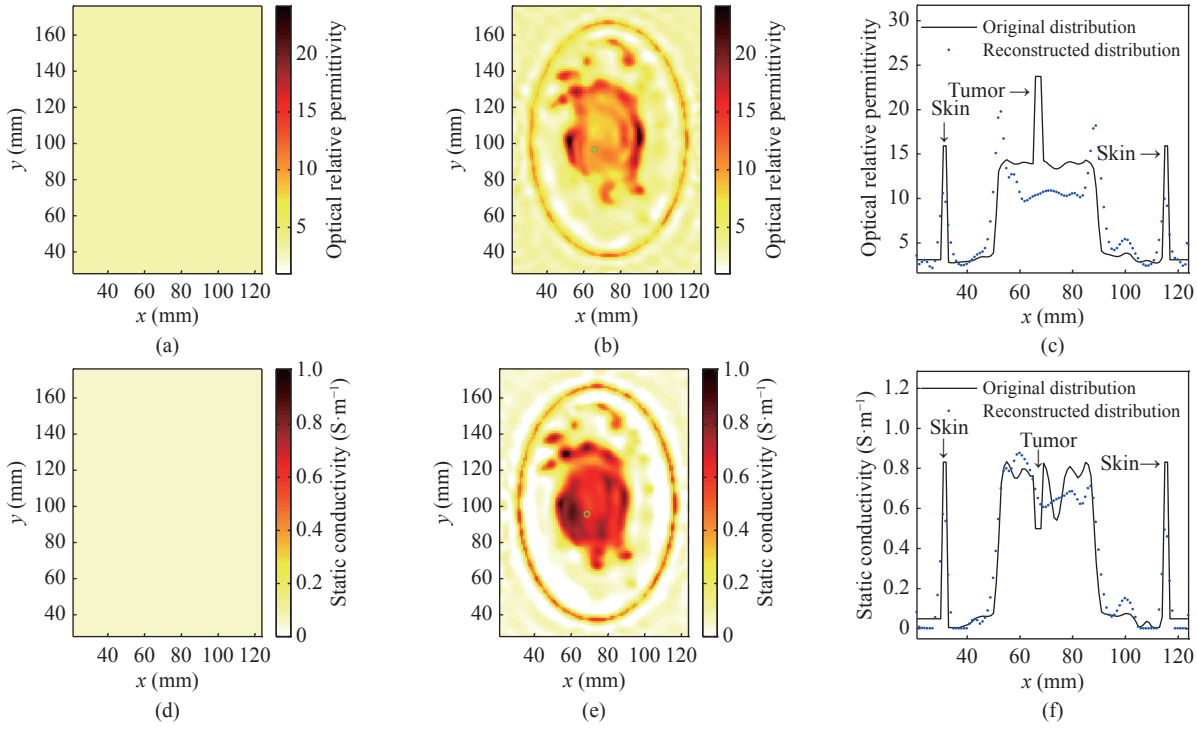

Fig. 17. (to be continued)

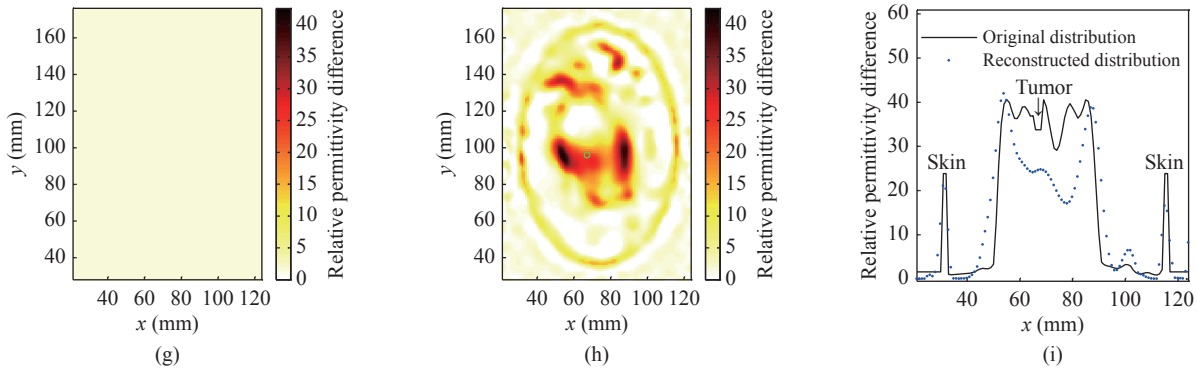

Fig. 17. Initial, reconstructed at the 300th iteration, and comparisons between original (black solid line) and reconstructed (blue dots) profiles on the x-axis through the tumor center for 2-D cancerous breast phantom **C** based on *Scenario II*: (a)–(c) ε_∞, (d)–(f) σ_s, and (g)–(i) $\Delta\varepsilon_1$. (continued)

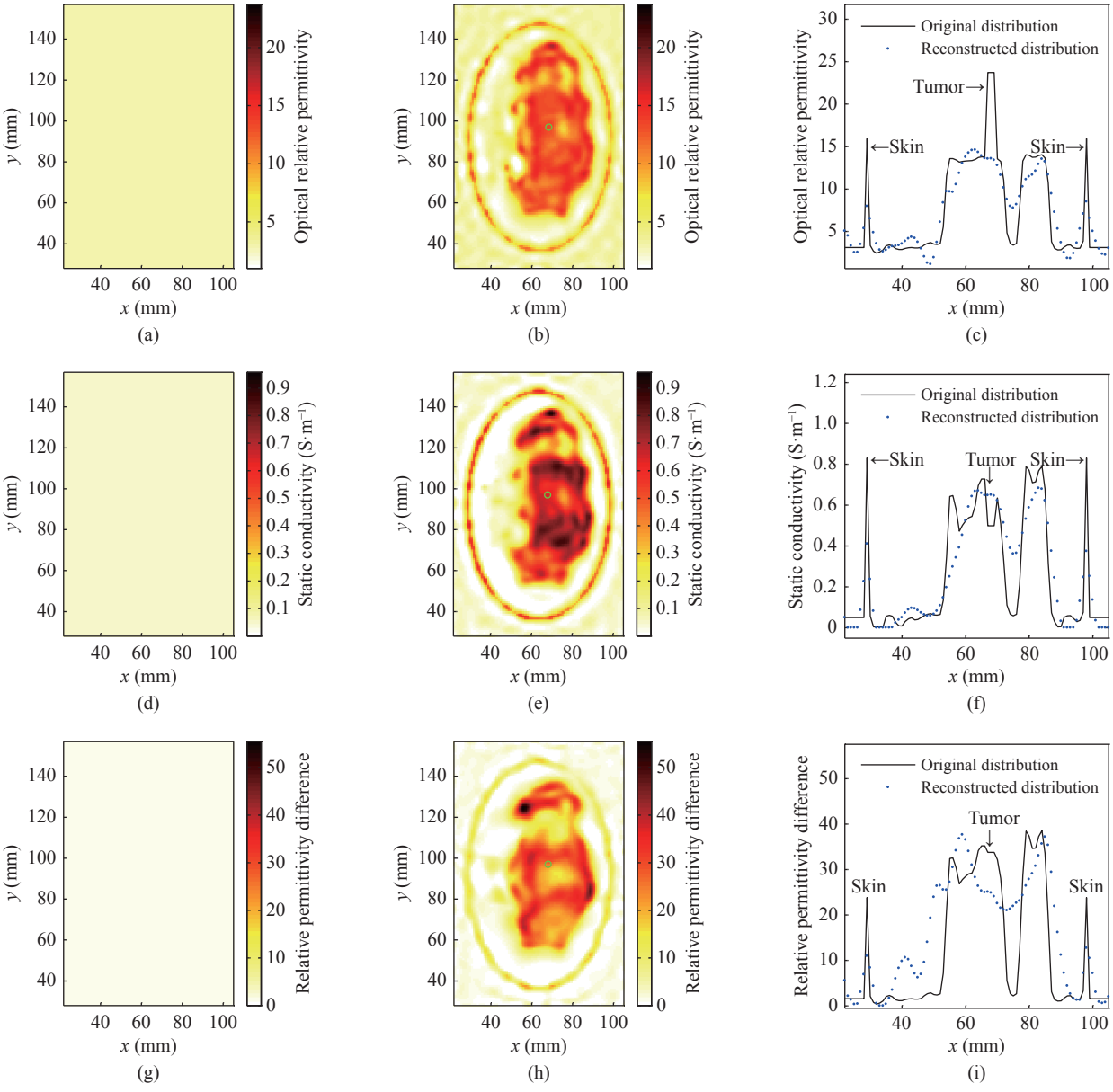

Fig. 18. Initial, reconstructed at the 300th iteration, and comparisons between original (black solid line) and reconstructed (blue dots) profiles on the x-axis through the tumor center for 2-D cancerous breast phantom **D** based on *Scenario II*: (a)–(c) ε_∞, (d)–(f) σ_s, and (g)–(i) $\Delta\varepsilon_1$.

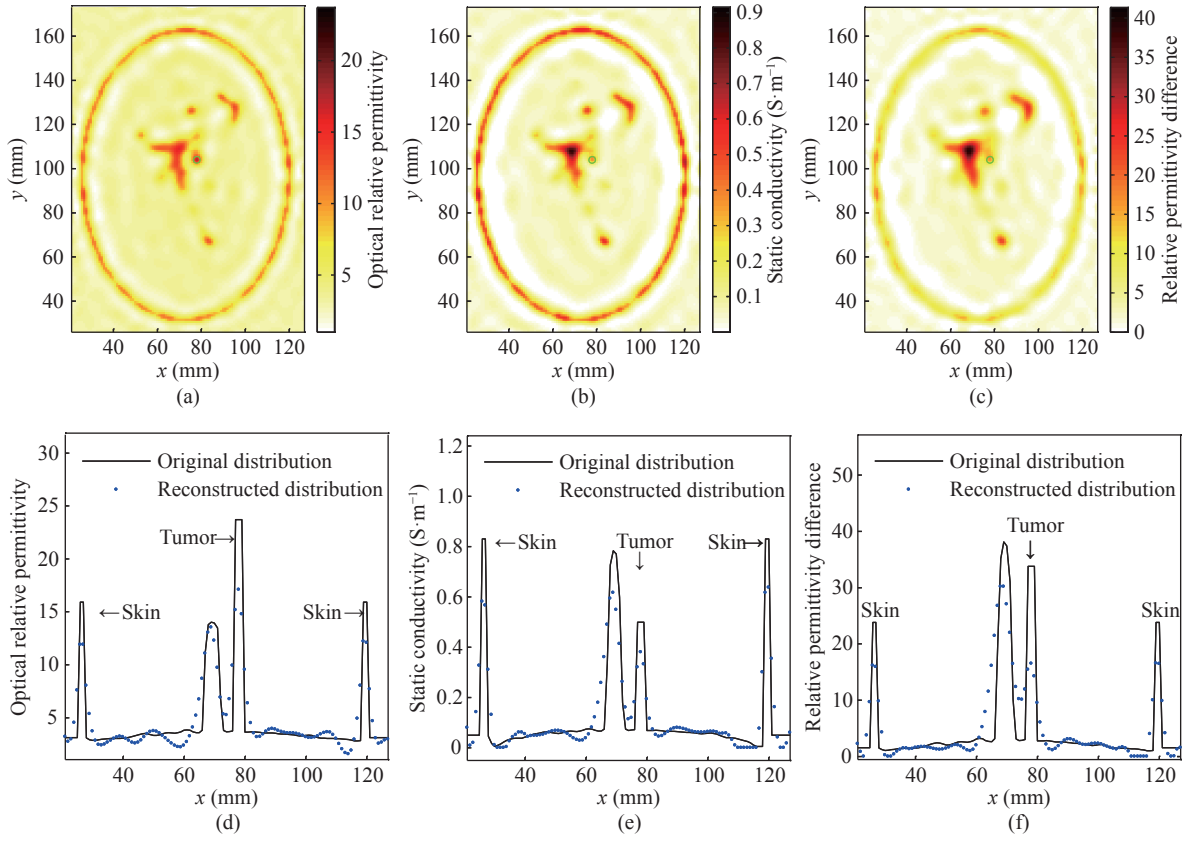

Fig. 19. Reconstructed distributions at the 300th iteration and comparisons between the original (black solid line) and reconstructed (blue dots) profiles on the x-axis through the tumor center in 2-D cancerous breast phantom **A** based on *Scenario III*: (a) and (d) ε_∞; (b) and (e) σ_s; (c) and (f) $\Delta\varepsilon_1$.

Fig.16 reveals that the three Debye model parameters are reconstructed satisfactorily within almost all of breast phantom in Scenario II and that the estimation accuracy of σ_s is the best, followed by that of $\Delta\varepsilon_1$, with that of ε_∞ being the worst, which is similar to Scenario I. Breast phantom B is similar to breast phantom A shown in Fig.16, where the imaging accuracy is decreased slightly. Fig.17 shows that the imaging quality of the skin is the highest, followed by that of normal tissues, and that of the tumor is the worst for breast phantom C. For breast phantom D, the reconstructed images shown in Fig.18 are seemingly poorer than those obtained with other breast phantoms.

Compared with Scenario I, the accuracy in reconstructing the three Debye model parameters within the skin region is lower for the four breast phantoms in Scenario II. This is a result of an application of less a priori information. However, the accuracies in reconstructing the three Debye model parameters within other regions are similar, which is due to the same initial estimates. Naturally, the tumor implanted in sparse breast phantoms is also detected successfully.

3. Scenario III

After 300 iterations, the reconstructed spatial distributions of the two-pole Debye parameters (similar results for $\Delta\varepsilon_2$ are omitted) in 2-D cancerous breast phantoms A, B, C, and D, based on Scenario III are shown in Figs.19, 20, 21, and 22, respectively. In these figures, the subgraphs (a) and (d), (b) and (e), as well as (c) and (f) give the estimated value and a comparison between the original (black solid line) and reconstructed (blue dotted line) profiles on the x-axis through its tumor center for ε_∞, σ_s, and $\Delta\varepsilon_1$, respectively. In particular, the respective additional green circles in subgraphs (a), (b), and (c) mark the location and size of the actual tumor.

Comparing between Figs.19–22 and Figs.15–18 (except initial distributions) shows that there are hardly any differences. Therefore, in Scenario III, the influence of the serious noise on imaging quality is effectively reduced by the Tikhonov's regularization scheme incorporated in our inverse scattering technique.

In addition, we also indicate the relative RMSEs versus the number of iterations in Fig.23, where their values (based on Scenario I, II, and III, respectively) are (0.2273, 0.5093, and 0.5108), (0.2371, 0.4752, and 0.4764), (0.4286, 0.4864, and 0.4809), and (0.2843, 0.3843, and 0.3778) for breast phantoms A, B, C, and D at the 300th iteration, respectively.

Figure 23 clearly shows that the relative RMSEs all decreased with the increase in the number of iterations

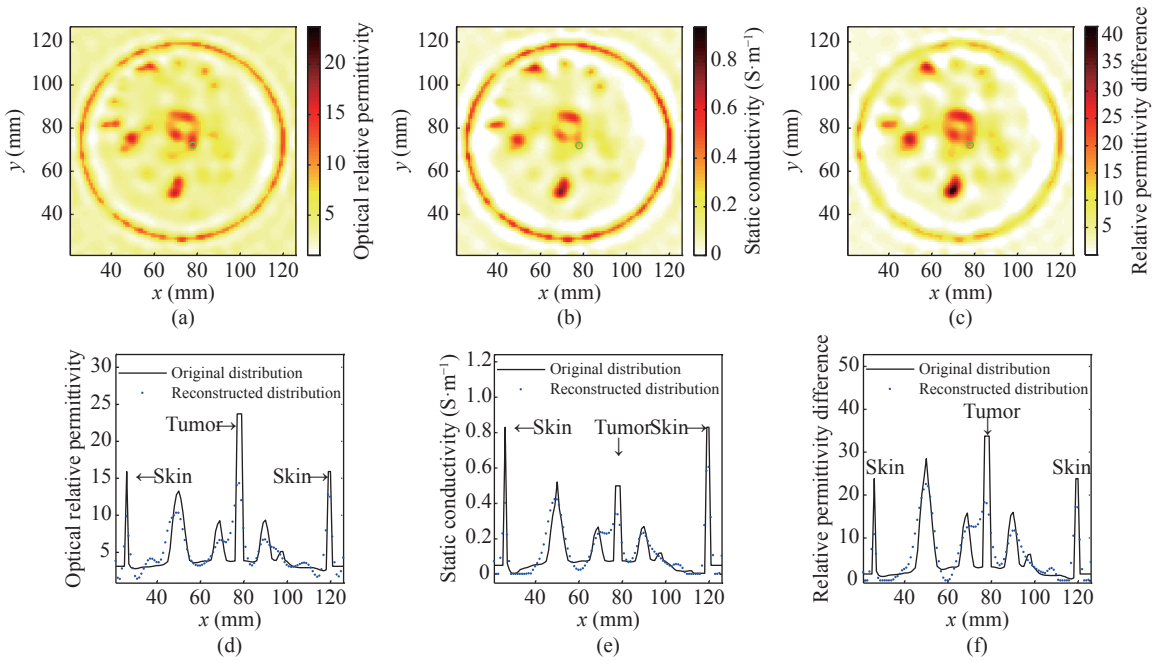

Fig. 20. Reconstructed distributions at the 300th iteration and comparisons between the original (black solid line) and reconstructed (blue dots) profiles on the x-axis through the tumor center in 2-D cancerous breast phantom **B** based on *Scenario III*: (a) and (d) ε_∞; (b) and (e) σ_s; (c) and (f) $\Delta\varepsilon_1$.

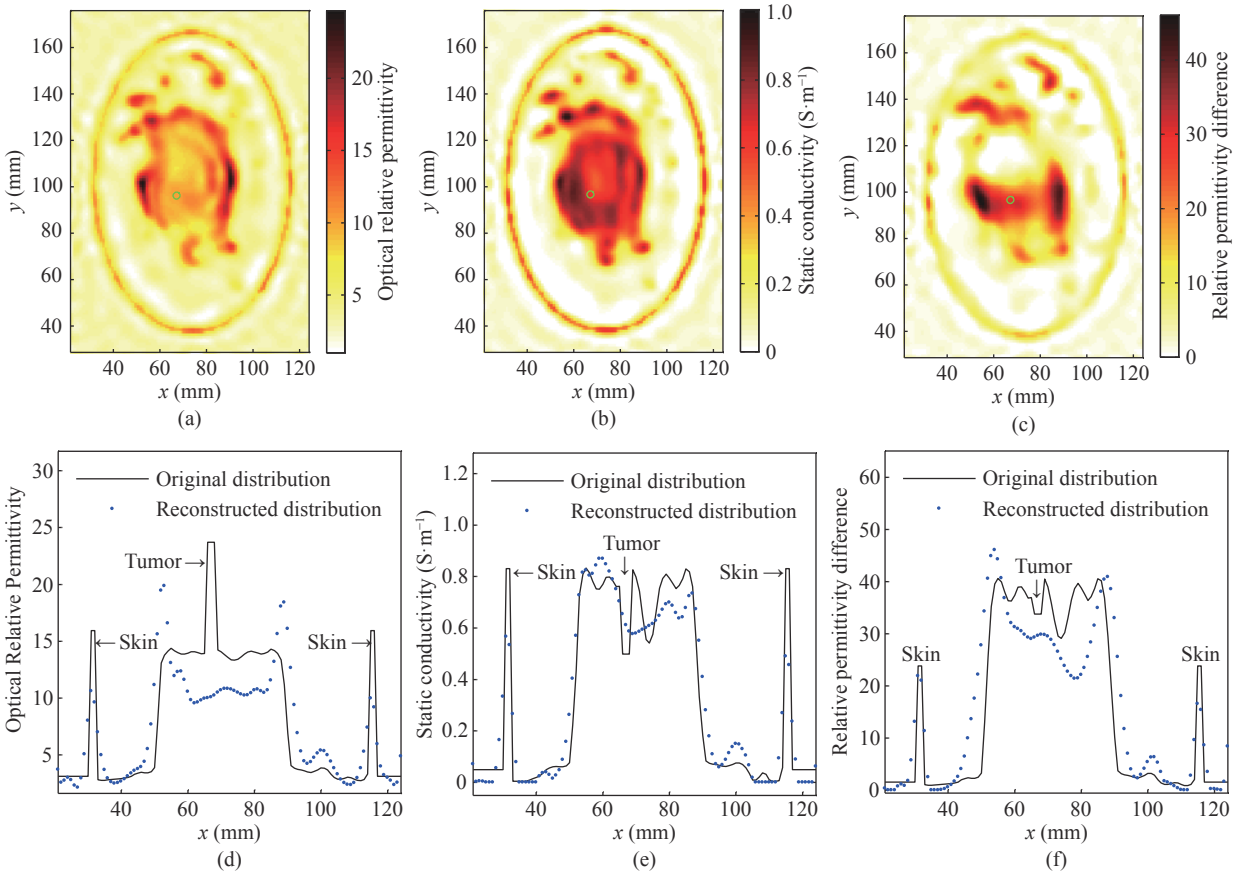

Fig. 21. Reconstructed distributions at the 300th iteration and comparisons between the original (black solid line) and reconstructed (blue dots) profiles on the x-axis through the tumor center in 2-D cancerous breast phantom **C** based on *Scenario III*: (a) and (d) ε_∞; (b) and (e) σ_s; (c) and (f) $\Delta\varepsilon_1$.

for the four breast phantoms in the three scenarios. Therefore, the presented microwave tomographic imaging algorithm is convergent in these cases, and some smaller reconstruction errors in practical clinical applic-

ations could be obtained by a proper increase in iterations. Furthermore, the comparison of errors among the three scenarios demonstrates that the reconstruction accuracy in Scenario I is the best, whereas that in Scenario II and that in III are similarly poor, for the four breast phantoms. The acceptable precision of reconstruction in Scenario III, where measurements are all contaminated by heavy noise, is thus beneficial from the incorporation of Tikhonov's regularization scheme in our algorithm. It could be further improved if more a priori information, such as the thickness of the skin, is provided. Additionally, the comparison of errors among four breast phantoms, shows that the computational accuracy for sparse breast phantoms is higher than that for dense breast phantoms in three scenarios. Generally, the calculation precision of phantom A in Scenario I is the best among them. Note, however, that these final errors should be decreased to an acceptable scope for practical clinical applications.

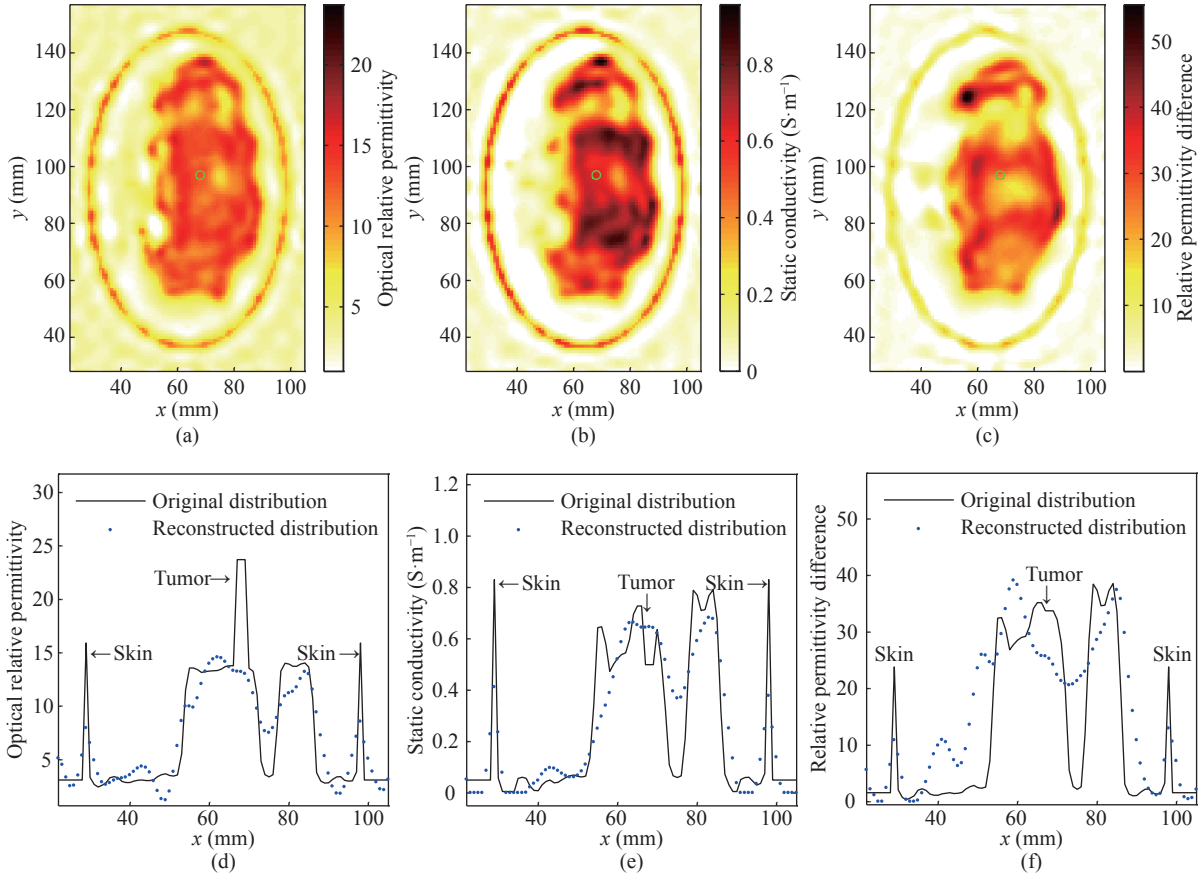

Fig. 22. Reconstructed distributions at the 300th iteration and comparisons between the original (black solid line) and reconstructed (blue dots) profiles on the x-axis through the tumor center in 2-D cancerous breast phantom **D** based on *Scenario III*: (a) and (d) ε_∞; (b) and (e) σ_s; (c) and (f) $\Delta\varepsilon_1$.

Furthermore, to further assess the performance of microwave tomographic imaging of anatomically realistic numerical phantoms with Debye dispersion for breast cancer detection using a regularized time-domain inverse scattering technique, the actual and reconstructed average Debye parameters and estimated relative RMSEs of the skin, fat, FG, transition, and tumor regions in three scenarios for four breast phantoms are given in Tables 2 and 3, respectively.

Again, Tables 2 and 3 illustrate that for different scenarios, the reconstruction quality in Scenario I is the best, but that in Scenario II and that in III are similarly poor for each breast phantom. Additionally, these results indicate that for different tissue regions, the reconstruction of the FG tissue is the most precise for each breast phantom, except in Scenario I, where that of the skin is the best due to its best initial estimate.

Finally, some practical issues are discussed. First, as discussed before, the improved TDIS algorithm is robust for four anatomically realistic breast phantoms in three scenarios. Second, the acceptable imaging accuracy provided by the algorithm is illustrated from the above reconstruction results. Finally, its time complexity is of great importance. At each iteration, two FDTD simulations are needed, and the average computational time executed on a PC with a four-core i5-2320 CPU

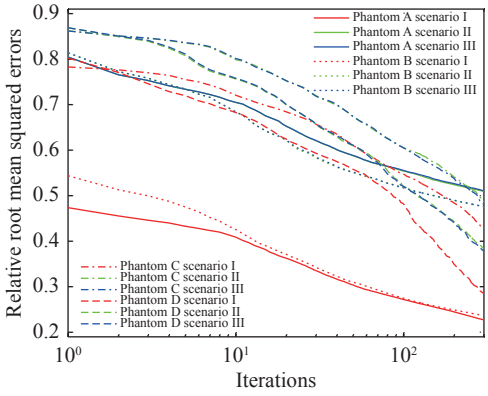

Fig. 23. Reconstructed relative RMSEs versus the number of iterations for four breast phantoms in three scenarios.

using MATLAB (R2011b, win64-bit) codes is 1.9 min/iteration for this 2-D case. When this proposed technique is, however, applied to large scale 3-D reconstructions, their high computational cost will become a new difficulty, which may be overcome by parallel processing or multifrequency techniques [16], [46], [47].

In summary, systemic research on the microwave tomographic imaging of four 2-D anatomically realistic cancerous numerical phantoms in three scenarios is carried out. The imaging results show that our algorithm is convergent for all these cases. The error analysis of the algorithm indicates that reconstruction error can be reduced by properly increasing a priori information and/or the number of iterations. The current imaging quality clearly reveals that the detection of breast tumors by the presented microwave tomographic imaging technique is promising for sparse breast tissue, but challenging for dense tissue. In addition, compared to some single-frequency methods, one of the advantages of the time-domain method proposed in this paper is that it can deal with dispersive media. One drawback of the time-domain method, however, is the increase in nonlinearity due to an increase in the number of unknowns, which decreases the chance of the method obtaining the global minimum. Therefore, it is still challenging to find a solution that is close to the exact one.

V. Conclusions and Future Work

The TDIS technique was improved from three aspects and then tested for the reconstruction of the spatial distribution of Debye parameters from four 2-D anatomically realistic breast models embedded in a 3 mm-diameter malignancy tumor, in three different scenarios. The obtained results demonstrate that the modified technique is feasible and promising for early-stage breast cancer detection and/or quantitative reconstruc-

Table 2. Actual and reconstructed average Debye parameters of skin, fat, FG, transition, and tumor regions in three scenarios for four breast phantoms

Phantom	Tissue	Average Debye parameters (ε_∞, σ_s (S/m), $\Delta\varepsilon_1$)			
		Actual values	Reconstructed values		
			Scenario I	Scenario II	Scenario III
A	Skin	(15.93, 0.83, 23.83)	(16.61, 0.86, 24.76)	(10.17, 0.46, 11.81)	(10.08, 0.46, 11.75)
	Fat	(3.32, 0.05, 2.06)	(3.38, 0.05, 2.27)	(3.58, 0.07, 2.77)	(3.59, 0.07, 2.77)
	FG	(13.59, 0.62, 31.93)	(11.10, 0.50, 22.73)	(11.07, 0.45, 21.41)	(11.00, 0.45, 21.33)
	Transition	(7.93, 0.22, 12.68)	(7.26, 0.24, 12.09)	(7.40, 0.24, 11.88)	(7.38, 0.24, 11.86)
	Tumor	(23.72, 0.50, 33.77)	(14.79, 0.42, 18.92)	(15.01, 0.32, 14.87)	(14.63, 0.32, 14.69)
B	Skin	(15.93, 0.83, 23.83)	(16.62, 0.86, 24.67)	(10.61, 0.47, 12.43)	(10.60, 0.47, 12.42)
	Fat	(3.33, 0.05, 2.10)	(3.45, 0.05, 2.48)	(3.70, 0.07, 3.14)	(3.70, 0.07, 3.15)
	FG	(13.78, 0.67, 33.84)	(12.26, 0.55, 26.20)	(12.35, 0.49, 23.50)	(12.36, 0.48, 23.43)
	Transition	(7.24, 0.19, 11.09)	(6.78, 0.19, 10.26)	(6.85, 0.20, 10.39)	(6.85, 0.20, 10.39)
	Tumor	(23.72, 0.50, 33.77)	(13.25, 0.37, 18.76)	(13.05, 0.32, 16.89)	(13.08, 0.31, 16.87)
C	Skin	(15.93, 0.83, 23.83)	(16.41, 0.85, 25.42)	(9.41, 0.45, 11.59)	(9.40, 0.45, 11.84)
	Fat	(3.22, 0.04, 1.86)	(3.47, 0.05, 2.23)	(3.87, 0.07, 3.43)	(3.87, 0.07, 3.45)
	FG	(13.84, 0.69, 34.70)	(11.19, 0.64, 12.98)	(10.83, 0.62, 14.88)	(10.71, 0.63, 16.33)
	Transition	(8.15, 0.23, 13.18)	(8.52, 0.29, 9.57)	(8.49, 0.30, 10.58)	(8.46, 0.31, 11.32)
	Tumor	(23.72, 0.50, 33.77)	(10.53, 0.72, 11.74)	(10.40, 0.65, 24.30)	(10.10, 0.62, 29.27)
D	Skin	(15.93, 0.83, 23.83)	(16.58, 0.85, 23.97)	(9.74, 0.47, 12.85)	(9.73, 0.47, 13.07)
	Fat	(3.11, 0.04, 1.65)	(3.47, 0.05, 3.61)	(4.04, 0.08, 4.63)	(4.05, 0.08, 4.53)
	FG	(13.82, 0.69, 34.55)	(12.93, 0.62, 27.01)	(12.73, 0.62, 24.96)	(12.63, 0.62, 25.85)
	Transition	(8.93, 0.25, 14.99)	(9.61, 0.35, 19.38)	(9.62, 0.36, 18.77)	(9.62, 0.36, 18.98)
	Tumor	(23.72, 0.50, 33.77)	(14.80, 0.63, 23.23)	(13.47, 0.65, 24.68)	(13.12, 0.64, 25.06)

Table 3. Reconstructed relative root mean squared errors of skin, fat, FG, transition, and tumor regions in three scenarios for four breast phantoms

Phantom	Tissue	Reconstructed error		
		Scenario I	Scenario II	Scenario III
A	Skin	0.0460	0.4494	0.4523
	Fat	0.3360	0.5668	0.5674
	FG	0.2748	0.3137	0.3154
	Transition	0.3848	0.3870	0.3869
	Tumor	0.3575	0.4444	0.4508
B	Skin	0.0536	0.4268	0.4276
	Fat	0.3241	0.5240	0.5262
	FG	0.2568	0.3077	0.3117
	Transition	0.3130	0.3233	0.3257
	Tumor	0.3982	0.4485	0.4523
C	Skin	0.0975	0.4729	0.4698
	Fat	0.4636	0.5299	0.5244
	FG	0.4394	0.4263	0.4161
	Transition	0.5404	0.5725	0.5916
	Tumor	0.5574	0.3346	0.3701
D	Skin	0.0940	0.4415	0.4384
	Fat	0.3857	0.5126	0.5096
	FG	0.2248	0.2627	0.2521
	Transition	0.5432	0.5708	0.5705
	Tumor	0.3219	0.3419	0.3434

tion of the internal breast composition, especially for sparse breast tissue. Future work will improve the TDIS algorithm to effectively detect dense breast tumors and test 3-D reconstruction problems.

References

[1] R. L. Siegel, K. D. Miller, H. E. Fuchs, *et al.*, "Cancer statistics, 2021," *CA:A Cancer Journal for Clinicians*, vol.71, no.1, pp.7–33, 2021.

[2] M. Jalilvand, X. Y. Li, L. Zwirello, *et al.*, "Ultra wideband compact near-field imaging system for breast cancer detection," *IET Microwaves, Antennas & Propagation*, vol.9, no.10, pp.1009–1014, 2015.

[3] S. Mukherjee, L. Udpa, S. Udpa, *et al.*, "A time reversal-based microwave imaging system for detection of breast tumors," *IEEE Transactions on Microwave Theory and Techniques*, vol.67, no.5, pp.2062–2075, 2019.

[4] H. Sato and S. Kidera, "ROI limited unknowns reduction-based contrast source inversion for microwave breast imaging," *IEEE Antennas and Wireless Propagation Letters*, vol.19, no.12, pp.2285–2289, 2020.

[5] X. Li, E. J. Bond, B. D. Van Veen, *et al.*, "An overview of ultra-wideband microwave imaging via space-time beamforming for early-stage breast-cancer detection," *IEEE Antennas and Propagation Magazine*, vol.47, no.1, pp.19–34, 2005.

[6] A. Zamani, A. M. Abbosh, and A. T. Mobashsher, "Fast frequency-based multistatic microwave imaging algorithm with application to brain injury detection," *IEEE Transactions on Microwave Theory and Techniques*, vol.64, no.2, pp.653–662, 2016.

[7] X. H. Zhang, X. L. Xi, M. C. Li, *et al.*, "Comparison of impulse radar and spread-spectrum radar in through-wall imaging," *IEEE Transactions on Microwave Theory and Techniques*, vol.64, no.3, pp.699–706, 2016.

[8] V. Gracheva and J. Ender, "Multichannel analysis and suppression of sea clutter for airborne microwave radar systems," *IEEE Transactions on Geoscience and Remote Sensing*, vol.54, no.4, pp.2385–2399, 2016.

[9] D. O'Loughlin, B. L. Oliveira, A. Santorelli, *et al.*, "Sensitivity and specificity estimation using patient-specific microwave imaging in diverse experimental breast phantoms," *IEEE Transactions on Medical Imaging*, vol.38, no.1, pp.303–311, 2019.

[10] H. Song, S. Sasada, N. Masumoto, *et al.*, "A two-stage rotational surface clutter suppression method for microwave breast imaging with multistatic impulse-radar detector," *IEEE Transactions on Instrumentation and Measurement*, vol.69, no.12, pp.9586–9598, 2020.

[11] J. E. Johnson, T. Takenaka, and T. Tanaka, "Two-dimensional time-domain inverse scattering for quantitative analysis of breast composition," *IEEE Transactions on Biomedical Engineering*, vol.55, no.8, pp.1941–1945, 2008.

[12] T. F. Yin, F. H. Ali, and C. C. Reyes-Aldasoro, "A robust and artifact resistant algorithm of ultrawideband imaging system for breast cancer detection," *IEEE Transactions on Biomedical Engineering*, vol.62, no.6, pp.1514–1525, 2015.

[13] G. Ruvio, R. Solimene, A. Cuccaro, *et al.*, "Comparison of noncoherent linear breast cancer detection algorithms applied to a 2-D numerical model," *IEEE Antennas and Wireless Propagation Letters*, vol.12, pp.853–856, 2013.

[14] A. Cuccaro, A. Dell'Aversano, G. Ruvio, *et al.*, "Incoherent radar imaging for breast cancer detection and experimental validation against 3D multimodal breast phantoms," *Journal of Imaging*, vol.7, no.2, article no.23, 2021.

[15] S. C. Hagness, A. Taflove, and J. E. Bridges, "Two-dimensional FDTD analysis of a pulsed microwave confocal system for breast cancer detection: fixed-focus and antenna-array sensors," *IEEE Transactions on Biomedical Engineering*, vol.45, no.12, pp.1470–1479, 1998.

[16] D. Oloumi, R. S. C. Winter, A. Kordzadeh, *et al.*, "Microwave imaging of breast tumor using time-domain UWB circular-SAR technique," *IEEE Transactions on Medical Imaging*, vol.39, no.4, pp.934–943, 2020.

[17] P. Mojabi and J. LoVetri, "A novel microwave tomography system using a rotatable conductive enclosure," *IEEE Transactions on Antennas and Propagation*, vol.59, no.5, pp.1597–1605, 2011.

[18] A. Fhager, M. Gustafsson, and S. Nordebo, "Image reconstruction in microwave tomography using a dielectric Debye model," *IEEE Transactions on Biomedical Engineering*, vol.59, no.1, pp.156–166, 2012.

[19] W. C. Chew and J. H. Lin, "A frequency-hopping approach for microwave imaging of large inhomogeneous bodies," *IEEE Microwave and Guided Wave Letters*, vol.5, no.12, pp.439–441, 1995.

[20] T. Takenaka, H. Jia, and T. Tanaka, "Microwave imaging of electrical property distributions by a forward-backward time-stepping method," *Journal of Electromagnetic Waves and Applications*, vol.14, no.12, pp.1609–1626, 2000.

[21] R. Solimene, A. Cuccaro, G. Ruvio, *et al.*, "Beamforming and holography image formation methods: an analytic study," *Optics Express*, vol.24, no.8, pp.9077–9093, 2016.

[22] D. W. Winters, E. J. Bond, B. D. Van Veen, *et al.*, "Estimation of the frequency-dependent average dielectric properties of breast tissue using a time-domain inverse scattering technique," *IEEE Transactions on Antennas and Propagation*, vol.54, no.11, pp.3517–3528, 2006.

[23] T. G. Papadopoulos and I. T. Rekanos, "Time-domain microwave imaging of inhomogeneous Debye dispersive scat-

terers," *IEEE Transactions on Antennas and Propagation*, vol.60, no.2, pp.1197–1202, 2012.

[24] M. Gustafsson and S. L. He, "A wave-splitting based optimization approach to multi-dimensional time-domain electromagnetic inverse problems," *Mathematics and Computers in Simulation*, vol.50, no.5-6, pp.541–551, 1999.

[25] I. T. Rekanos, "Time-domain inverse scattering using Lagrange multipliers: an iterative FDTD-based optimization technique," *Journal of Electromagnetic Waves and Applications*, vol.17, no.2, pp.271–289, 2003.

[26] M. A. Ali and M. Moghaddam, "3D nonlinear super-resolution microwave inversion technique using time-domain data," *IEEE Transactions on Antennas and Propagation*, vol.58, no.7, pp.2327–2336, 2010.

[27] M. Lazebnik, M. Okoniewski, J. H. Booske, *et al.*, "Highly accurate Debye models for normal and malignant breast tissue dielectric properties at microwave frequencies," *IEEE Microwave and Wireless Components Letters*, vol.17, no.12, pp.822–824, 2007.

[28] S. Gabriel, R. W. Lau, and C. Gabriel, "The dielectric properties of biological tissues: III. Parametric models for the dielectric spectrum of tissues," *Physics in Medicine & Biology*, vol.41, no.11, pp.2271–2293, 1996.

[29] P. Charbonnier, L. Blanc-Féraud, G. Aubert, *et al.*, "Deterministic edge-preserving regularization in computed imaging," *IEEE Transactions on Image Processing*, vol.6, no.2, pp.298–311, 1997.

[30] R. A. Willoughby, "Solutions of ill-posed problems (A. N. Tikhonov and V. Y. Arsenin)," *SIAM Review*, vol.21, no.2, pp.266–267, 1979.

[31] UWCEM, "Phantom repository," Available at: https://uwcem.ece.wisc.edu/phantomRepository.html, 2021.

[32] D. Colton and R. Kress, *Inverse Acoustic and Electromagnetic Scattering Theory*. Springer, New York, NY, USA, pp.7–12, 2013, doi: https://doi.org/10.1007/978-1-4614-4942-3.

[33] I. T. Rekanos and A. Raisanen, "Microwave imaging in the time domain of buried multiple scatterers by using an FDTD-based optimization technique," *IEEE Transactions on Magnetics*, vol.39, no.3, pp.1381–1384, 2003.

[34] P. C. Hansen, "Analysis of discrete ill-posed problems by means of the L-curve," *SIAM Review*, vol.34, no.4, pp.561–580, 1992.

[35] J. Nocedal and S. J. Wright, *Numerical Optimization*. Springer, New York, NY, USA, pp.497–525, 2006, doi: 10.1007/978-0-387-40065-5.

[36] H. Sagan, *Introduction to the Calculus of Variations*. McGraw-Hill, New York, NY, USA, pp.10–22, 1969.

[37] Y. H. Dai, "A family of hybrid conjugate gradient methods for unconstrained optimization," *Mathematics of Computation*, vol.72, no.243, pp.1317–1329, 2003.

[38] A. Taflove and S. C. Hagness, *Computational Electrodynamics: The Finite-Difference Time-Domain Method*, 3rd ed., Artech House, Boston, MA, USA, pp.353–368, 2005.

[39] J. A. Roden and S. D. Gedney, "Convolution PML (CPML): an efficient FDTD implementation of the CFS-PML for arbitrary media," *Microwave and Optical Technology Letters*, vol.27, no.5, pp.334–339, 2000.

[40] C. T. Kelley, *Iterative Methods for Optimization*. SIAM, Philadelphia, PA, USA, pp.40–49, 1987.

[41] S. K. Davis, H. Tandradinata, S. C. Hagness, *et al.*, "Ultrawideband microwave breast cancer detection: a detection-theoretic approach using the generalized likelihood ratio test," *IEEE Transactions on Biomedical Engineering*, vol.52, no.7, pp.1237–1250, 2005.

[42] E. Zastrow, S. K. Davis, M. Lazebnik, *et al.*, "Development of anatomically realistic numerical breast phantoms with accurate dielectric properties for modeling microwave interactions with the human breast," *IEEE Transactions on Biomedical Engineering*, vol.55, no.12, pp.2792–2800, 2008.

[43] American College of Radiology, *Breast Imaging Reporting and Data System Atlas (BI-RADS Atlas)*. ACR, Reston, VA, USA, 2003.

[44] T. C. Williams, E. C. Fear, and D. T. Westwick, "Tissue sensing adaptive radar for breast cancer detection-investigations of an improved skin-sensing method," *IEEE Transactions on Microwave Theory and Techniques*, vol.54, no.4, pp.1308–1314, 2006.

[45] D. W. Winters, J. D. Shea, E. L. Madsen, *et al.*, "Estimating the breast surface using UWB microwave monostatic backscatter measurements," *IEEE Transactions on Biomedical Engineering*, vol.55, no.1, pp.247–256, 2008.

[46] G. D. Liu, "Time-domain electromagnetic inversion technique for biological tissues by reconstructing distributions of Cole-Cole model parameters," *Applied Computational Electromagnetics Society Journal*, vol.32, no.1, pp.8–14, 2017.

[47] Q. Q. Fang, P. M. Meaney, and K. D. Paulsen, "Microwave image reconstruction of tissue property dispersion characteristics utilizing multiple-frequency information," *IEEE Transactions on Microwave Theory and Techniques*, vol.52, no.8, pp.1866–1875, 2004.

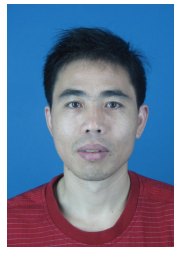

LIU Guangdong (corresponding author) was born in Jiangsu, China, in 1972. He received the Dr. Eng. degree in electromagnetic field and microwave technology, from the College of Electronic Science and Engineering, Nanjing University of Posts and Telecommunications, in 2011. Currently, he is a Professor of the School of Electrical and Control Engineering, Nanjing Polytechnic Institute, China. His research interests include electromagnetic inverse scattering theory and its applications. (Email: gdliu@njpi.edu.cn)